Thesis for the degree
Master of Science

Submitted to the Scientific Council of the
Weizmann Institute of Science
Rehovot, Israel

עבודת גמר (תזה) לתואר
מוסמך למדעים

מוגשת למועצה המדעית של
מכון ויצמן למדע
רחובות, ישראל

By
Lior Gazit

מאת
ליאור גזית

משוב קוונטי ביונים לכודים
Quantum feedback on trapped ions

Advisor:
Prof. Roee Ozeri

מנחה:
פרופ' רועי עוזרי

May 2020

אייר התש"פ

To Tammy Langer & Edward Gaunt (1937-2020)

Acknowledgment

This work could not have been done without the support, patience, wise advice, kindness, and good friendship of several people. I would like to start by thanking the 185 lab team: Nitzan Ackerman, Ravid Sahniv, Tom Manovitz, Lee Peleg, and Yotam Shapira for their endless patience, explaining, teaching, and always consulting with a smile and endless kindness. Thanks for the countless hours spent together in the lab, or outside of it, thinking of solutions, talking, laughing, and just being good friends. I would like to thank the rest of the trapped ions group: Ruti, Meirav, Meir, Yonathan, David, Haim & Sapir for their interest, ideas, conversations, kindness, and friendship. Moreover, I would like to express my love and gratitude to my parents for their endless support in every step I take, my brothers and sister, for making my life funnier. For my partner, Gal for understanding, encouraging, and always asking questions. Also, Dor, Pavel, and Ido - thank you for studying beside me for the past two and a half years. Thanks for your intelligence, friendship, being a shoulder to cry on, and always putting things in perspective. Finally, I want to thank my advisor Prof. Roee Ozeri for his patience, clever questions, and mentoring and teaching me a new way of thinking.

Abstract

To realize and scale up a quantum information device, the implementation of quantum error correction codes will be inevitable. The use of measurement of the quantum correlations between qubits to detect the errors, and correcting them using conditional feedback, is fundamental to the experimental realization of such a device. The following thesis reports on characterization, construction, and integration of an online analysis and feedback system for $^{88}Sr^{+}$ions held in a linear Paul trap. Prior to this work, the analysis of the ion state was done offline, using post-processing of images taken from an EMCCD camera at the end of each experiment. This work presents a new addition to our lab that allows live readout from the EMCDD, online analysis of the register state using a Camera Link protocol. This process is followed by an flexible in-sequence feedback operation. We have demonstrated this ability on one and two ion-qubits: on one ion-qubit, we have initialized it in an equal superposition, then, a measurement was followed by a conditional π pulse only if the qubits measurement result was a dark state; thus, the qubit always ended up in a bright state with 98.6% fidelity. Using two ion-qubits, live readout and feedback was tested and demonstrated using a conditioned Ramsey experiment on superimposed qubits with $\sim$ 82% fidelity. Next using two ion-qubits, we have demonstrated quantum feedback. The quantum feedback was done by measuring one of two entangled qubits in the $\hat{x}$ basis. This measurement collapsed the second ion to a superposition state also in the $\hat{x}$ basis. The measurement was followed by a conditional Ramsey sequence, achieving quantum feedback fidelity of $\sim$ 85%. Moreover, in this work, we introduced a new set of tools that are now available in our lab: (a) Selective readout (or "hiding") where the qubits superposition is hidden during the measurement thus remaining coherent despite the presence of a laser resonant with an atomic dipole transition; (b) dynamical decoupling using RF pulses while the qubit is in hiding; and (c) individual addressing with negligible cross-talk due to the use of light shift instead of a $\hat{\sigma_x}$ rotation.

Contents

1 Introduction

"Probably never before has a theory been evolved which has giving a key to the interpretation and calculation of a heterogeneous group of phenomena of experience as has quantum mechanics theory"

—Albert Einstein, Out of my latter years.

Quantum mechanics describes the behavior of matter and light as a whole. On the atomic scale, the behavior of things can be very peculiar and counter-intuitive. Atomic physics is one of the tools that can help us to understand quantum mechanics better. This understanding can be achieved by the ability to perform experiments and to control quantum systems. These kinds of experiments are fundamentally hard - the quantum mechanical phenomena that we are interested in controlling are highly sensitive to noise such that can lead to loss of information, a procedure known as decoherence.

Trapped ions in a Paul trap are highly controllable systems yet well isolated. Moreover, the fact that an ion is inherently a quantum mechanical creature that can be controlled, cooled, and entangled contributes to the fact that this is a leading platform for quantum mechanics experiments.

Quantum information processing (QIP) exploits the quantum mechanics principles such as superposition and entanglement for different computational tasks. A building block of QIP is the qubit - a quantum mechanical description of a bit. A classical bit of information can take one of two states, 0 or 1, whereas the qubit is represented by a unit vector in a 2-dimensional complex plane. The significant difference comes from the fact that N qubits are represented by a unit vector in a 2^n-dimensional complex plane. The exponential growth in size is necessary to take into account not just the state but the correlation of the amplitude and phase of a superposition. These correlations can be utilized to describe new types of computation algorithms that can efficiently solve some problems that classical computers cannot efficiently solve. Quantum information can be used as a platform for a variety of applications: Quantum simulation, quantum cryptography, precision measurement, and quantum algorithms.

In order to perform a quantum information task, one needs to have the ability to perform any possible rotation in the 2^N dimensional Hilbert space. Moreover, the ability to read out the quantum state of a register such that each state is uniquely identified is also necessary. In order to perform a conditional QIP tasks, where the operation depends on the outcome, one must have the ability to read

the register state fast enough before it will decohere, and also to be able to act upon selected scenarios.

In trapped ions, these requirements are achievable but challenging. The readout of a qubit state (where each qubit is an ion) is done mainly using the detection of fluorescence from the ion, using a detection scheme known as state selective fluorescence. The fluorescence is detected using an EMCCD camera. The fluorescence detection time has to be (a) sufficiently long to collect enough light to be able to discriminate between states (exposure time) and (b) sufficiently fast to allow for many iterations within the coherence lifetime of the ion. To meet these requirements, the camera readout and state analysis need to be performed in real-time and within the coherence time of the ions. The ability to read out the register state and to act according to its state before the ions decohere is a prerequisite for experiments that require live feedback such as quantum error correction.

This thesis will review the construction, integration, and testing of an online readout system combined with a feedback system for an existing apparatus of $^{88}Sr^{+}$ ions. Before this system, the state analysis of the ions state was done offline using Matlab, and quantum feedback was not possible. Our solution was implemented using a dedicated FPGA frame grabber card that is connected using a Camera Link protocol to and EMCCD camera that allows online access to the raw image data and fast image analysis.

2 Background and theory

2.1 Motivation

Quantum information processing is the result of combining quantum physics with computing theory. Harnessing the properties of the Hilbert space structure of quantum physics, superposition and entanglement introduce a variety of operations that have no classical concept. The origin of quantum computations starts with two people in the early 1980s, one of them being Richard Feynman, who asked - how to simulate quantum mechanics on a classical computer. This task is hard, and not trivial due to the exponential increase in degrees of freedom. He was the first to suggest a computer made of quantum particles. David Deutsch is the second pioneer, who suggested building a universal quantum computer out of a Turing machine. In 1995 Peter Shor proposed a quantum algorithm for integer factorization in polynomial time as opposed to sub-exponential time used in a classical computer. This was the first suggestion that a quantum computer can out-preform a classical computer [1]. The existence of a polynomial-time quantum algorithm for factorization suggests that one of the most widely used cryptographic protocols (RSA) is vulnerable to an adversary who possesses a quantum computer.

The fundamental building block of QIP is the quantum bit (qubit), the quantum analog to the classical bit. The qubit is a two-level quantum system, usually denoted as $|0\rangle$ and $|1\rangle$. Most QIP involves manipulating, controlling, and measuring a register of a qubit(s). Quantum gates are the basic quantum circuit operating on a small set of qubits, similar to classical gates except for the fact that quantum gates are unitary operators meaning they are time reversal. Qubits and quantum gates are the elements that build a quantum computer - a fully digitized controllable QIP machine. There are a set of requirements that a system needs to meet in order to realize a quantum computer, they were listed by David DiVincenzo in 1998 and are known as the **five DiVincenzo criteria** [2] . They include:

- A scalable physical system with well-characterized qubits
- The ability to initialize the state of the qubits to a simple fiducial state, such as $|00...0\rangle$.
- Long relevant coherence time, much longer than the gate operation time.
- A "universal" set of quantum gates.
- A qubit specific measurement capability

The essence of these criteria combine universality, long coherence times and scalability. It has been shown that single qubit rotations and two qubit controlled-NOT gate constitute of a universal gate set. However, when trying to coherently control many qubits or maintaining long coherence times in a noisy environment, the implementation of these operations, especially entanglement, is greatly reduced.

Trapped ions are long known to be a promising platform for constructing quantum devices with excellent coherent control capabilities and very long coherence times [3]. In 1995, Cirac and Zoller [4] proposed an architecture of a quantum computer based on trapped ions. The qubit can be encoded in the internal state of the trapped ion. Using tightly focused laser beams, the state of an individual ion (or ions) in the string can be rotated, and the interaction between two ions can be performed by coupling the motional modes to the internal ion state to implement an entangling gate thus satisfying the universal gate set. The rest of the DiVincenzo criteria accomplished using trapped ions as well: optical pumping and laser cooling [5] satisfy the ability to initialize the qubit state, long coherence time is a property of trapped ions which are highly isolated from the environment and can be nicely demonstrated in highly stable atomic clock experiments, electron shelving and on resonance fluorescence are the measuring scheme.

However, the fidelity of all of the above operations is not perfect - achieving complete isolation from the environment is a hard task. Furthermore, the scalability of the quantum computer critically depends on the fidelity of quantum coherent control. It is agreed that active error correction methods will be the solution to overcome these problems.

While quantum error correction (QEC) will be thoroughly discussed in the next section, the fact that QEC codes all rely on imperfect entangling gates gives rise to the fact that a noisy quantum computer may simulate a noise-less but smaller quantum computer as long as the noise level is below a certain threshold - the well-known fault-tolerance theorem [6]. This, among other breakthroughs in the field, has motivated work towards optimizing QEC methods. Although some proof of concept experiments where implemented, including a new demonstration of quantum supremacy by Google [7], realizing a large scale quantum computer is still an ongoing effort.

One of the most vital theoretical aspects of QIP are Quantum Error Correction (QEC) and fault-tolerant quantum computation. A qubit lives in a very hostile environment. For example vibrations (thermal phonons) can stir the qubit state, stray photons can flip the qubit state, relaxations and spontaneous scattering can send the qubit back to its ground state ,and a measurement will turn the qubit into no more than a conventional classical bit. All of these render the

survival of a single qubit superposition over long times unlikely. Quantum error correction codes use groups of qubits, teamed up to mitigate the harmful effects of the environment. By using these kinds of codes, performing complex quantum computations without losing coherence becomes possible. In order to do so, the interactions between the qubits need to follow well-structured fault-tolerant protocols. The basics of quantum error correction and fault-tolerant quantum computation were first introduced in 1995, as a result of interest in quantum computations, following up the 1994 Shor's factorization algorithm.

The theoretical results showed that building a large scale quantum computer is in principle possible. The fault-tolerant approach is the most general approach to correct errors. It has shown that for a long computation, it can correct arbitrary errors (where the error threshold is 10^{-4}) for a single gate operation. Classical error correction protects information using redundancy. In quantum mechanics, the no-cloning theorem states that an unknown state cannot be cloned, making classical QEC through redundancy non-trivial. Luckily, encoding the information on entangled states can protect it. QEC codes, use the fact that information can be encoded into a subspace of a larger Hilbert space. A "smart" measurement, will collapse the wave function into one of two orthogonal subspaces - one where the error is corrected, or to an orthogonal subspace that outputs a syndrome that can be used to correct the error.

Quantum error correction requires not only the ability to manipulate the qubits via universal gate sets, but also the ability to perform smart measurements, and correct the errors (if needed) before the system completely decohere. It can correct trace-preserving errors but also errors that are not trace-preserving like measurement. This implies that the use of live feedback is needed in order to perform tasks that will allow the implementation of quantum error correction codes. The following section review the solutions and experiments that have been proposed and tests for implementing QEC on trapped ions.

2.2 Literature review

quantum error correction and feedback in trapped ions

QEC codes have been demonstrated in several quantum information platforms, from superconducting qubits, nuclear magnetic resonance (NMR) systems, and trapped ions. The first protocols demonstrated error syndrome measurement outside of the qubit subspace. Von Neumann projective measurements of multi-qubit operators are required [8]in order to achieve practical QEC on continuously encoded information. These have been realized with trapped ions [9, 10, 11], and in

solid-state systems [12].

Implementation of quantum error correction codes is done by coding the quantum state such that after a measurement and feedback, the errors are erased. In these procedures, using a larger subspace of the Hilbert space, errors will rotate the state vector out of the allowed subspaces, where measurement will project it back to the allowed subspace, and the original state will be recovered. The first implementation of quantum error correction codes was in NMR systems [13, 14].

A reduction of high intrinsic or artificially induced errors in logical qubits has been demonstrated in several experiments. However, fault-tolerant encoding of logical qubit has not been shown yet. The next paragraph will discuss some of the QEC experiments demonstrated in trapped ions systems.

In 2004 [15], used trapped ions to implemented a fundamental quantum error correction protocol. The authors encoded the (arbitrary) state of a source qubit in a superposition of two distinct three-qubit states (logical plus two auxiliary qubits). They had introduced controlled spin-flip errors on all three ion-qubits before they encoded the state with the inverse operation used to encode the logical qubit. Small errors in the encoded state will rotate the states in a way that the errors can be corrected after decoding. The readout of the auxiliary qubits provided the error syndrome, based on which, the logical ion-qubit was rotated to its original state. The stabilizer code $\{ZZX, ZXZ\}$ was employed in these experiments. With no error, the fidelity was around 0.8, in an uncorrected state, the fidelity dropped to 0.5. In this experiment, they used individual addressing, through ion-shuttling between different trapping regions, for the preparation of the ion, and selective state readout for detecting the error syndrome.

In 2011 Schindler et al. have demonstrated repeated QEC with three $^{40}Ca^{+}$ ions [10]. This experiment characterized the implementation of the QEC process in the presence of correctable errors, and concluded that QEC protocol corrects single-qubit errors within their statistical uncertainty. The fidelity depended on the number of QEC code repetitions, where for one sequence, they have reached 90%. Following this work in 2014, the same Innsbruck group introduced an implementation of topological 7 qubit code [9]. This was the first realization of a complete Calderbank-Shor-Steane (CSS) code. In this work, they have constructed a topological color code using seven trapped ions that encoded a single logical qubit.

Recently, the $[[4, 2, 2]]$ code implemented by [16] on a fully connected quantum computer, including a chain of five $^{171}Yb^{+}$ ions confined in a Paul trap. This surface code is a quantum error detection code [17], contains two logical qubit constructed out of four ions. This is a one qubit fault-tolerant code where one of

the qubits is protected ($|L_a\rangle$), and the other is not. By instead considering errors on both encoded qubits, they have highlighted the importance of fault-tolerance for reducing intrinsic errors and managing error propagation. The non–fault-tolerant procedures that generate the non-protected logical qubits ($|L_b\rangle$ still succeed in reducing added errors. The code implements $|L_a\rangle$ and $|L_b\rangle$ on only four physical qubits and hence violates the quantum Hamming bound [18], which means that detected errors cannot be uniquely identified and corrected. Therefore they rely on post-selection to find and discard cases where an error occurred. The code does have the advantage of requiring only five physical qubits for the fault-tolerant encoding of $|L_a\rangle$: four data qubits and one ancilla qubit.

Not all of the above experiments demonstrated conditioned operations on the qubits. Some of them have used post-selection to match the outcome of the measurement and the desired operation. The implementation of high-fidelity, large scale systems with the ability to perform consecutive measurements appears to be challenging.

Continuous and conditioned operation after measurement on trapped ions was presented in a few experiments. One of them is correcting photon scattering errors in atomic qubits [19]. In this experiment, polarized photons scattered from a Zeeman qubit on the $\hat{x}$ direction (perpendicular to the quantization axis) were collected, using two photomultiplier tubes (PMT) and two polarizing beam splitters (PBS). By analyzing which PMT detected the signal with a recording of the local oscillator phase, they could correct any kind of scattering error. Conditional operation using a CCD camera has been demonstrated in [20].

Some of the experiments described above used methods such as hiding the data qubit in an internal state that does not interact with the light used for detection. An alternative approach that also use feedback to utilize quantum error correction is to use two species qubits [21]. They have obtained high degree of spectral isolation using the fact that one of the species is the auxiliary qubit, and one is the data qubit. The information is transferred in the register from the qubit and the auxiliary using mixed-species multi-qubit gates, enabling state detection without crosstalk to the data qubits. A key element of the experimental setup is a classical control system with an in-sequence feedback control. The readout of the ion state was done using a PMT. Recently, more works are using live feedback in order to perform different QEC codes experiments such as [22, 23]. Most of them are not in a trapped ions systems or using an EMCCD camera, and are out of the scope of this work.

2.3 Theory

2.3.1 Ion - light interaction

In our experiment, trapped ions are interacting with a classical electromagnetic field created by a laser. We can think of the ion as a Hydrogen-like ion - a charged atom with one electron in the valance shell. We will assume that all other electrons remain in a fixed state such that the only degrees of freedom are those of the valence electron and the center of mass coordinates of the ion. To determine how the trapped ions act as qubits, we will consider the ion as an effective two-level system since the interaction with the EM field is perturbative. The dynamics will involve only the levels which are in resonance with the interaction. This yields the effective Hamiltonian:

$$\hat{H}(t) = \hat{H}_{ion} + \hat{V}_{Ion-Laser}(t)$$

$\hat{H}_{ion}$ is the free Hamiltonian of a spin $\frac{1}{2}$ connected to a $1D$ harmonic oscillator:

$$\hat{H}_{ion} = \frac{1}{2}\hbar\omega_0\sigma_z + \hbar\nu\left(\hat{a}^\dagger\hat{a} + \frac{1}{2}\right)$$

here, ω_0 is the frequency separation of the qubits levels, and ν is the harmonic oscillator frequency.

The time-dependent periodic potential $\hat{V}(t)$ is induced by coupling to the e.m. wave:

$$\hat{V}_{IL}(t) = \hbar\Omega_0\left(\hat{\sigma}^+ + \hat{\sigma}^-\right)cos\left(k\hat{x} - \omega_L t + \phi\right)$$

Ω_0 is the coupling constant known as the Rabi frequency, k is the wavenumber, $\hat{\sigma}^\pm$ is the spin rising\lowering operators that act on the internal atomic state (in our case $|S\rangle$ and $|D\rangle$) defined as: $\sigma^\pm = \hat{\sigma}_x \pm i\hat{\sigma}_y$.

The position operator can be written in terms of the harmonic oscillator ladder operators:

$$k\hat{x} = kx_{eq} + \eta\left(a^\dagger + a\right)$$

Where $\eta = kx_0 = k\left(\frac{\hbar}{2m\omega_m}\right)^{1/2}$ is the Lamb-Dicke parameter, and x_0 is the ground state width of the harmonic oscillator.

Moving to the interaction picture with respect to H_{ion} using $U = e^{iH_0 t/\hbar}$, and neglecting fast terms (which oscillates at $\omega_L + \omega_0$) in the rotating wave approximation (RWA) we can write the Hamiltonian as:

$$H_{int} = UHU^{\dagger}$$

$$H_{int}(t) = \frac{\hbar\Omega}{2}\sigma^{+}e^{i\eta\left(\hat{a}e^{(-i\nu t)}+\hat{a}^{\dagger}e^{(i\nu t)}\right)} \cdot e^{i(\phi-\delta t)} + h.c.$$

with $\delta = \omega_L - \omega_0$.

The laser couples the state $|S,n\rangle$, to all states $|D,m\rangle$ (n is the vibrational quantum number). This coupling is due to the oscillatory motion of the ion in the trapping potential. Increasing or decreasing of the vibrational quantum number is a result of the absorption or emission process on a sideband of the electronic transition that satisfies energy conservation. By expanding the exponent $e^{i\eta\cdots}$ (Assuming $\eta \ll 1$) we get the Hamiltonian

$$(1)\ \ H_{int} = \frac{\hbar\Omega}{2}\hat{\sigma}^{+}\left(1 + i\eta\left(\hat{a}e^{(-i\nu t)} + \hat{a}^{\dagger}e^{(i\nu t)}\right)\right)e^{-i(\phi+\delta t)} + h.c.$$

We can see that the coupling of the $|n\rangle$ level to the $|m\rangle$ level of the harmonic oscillator is obtained by terms oscillating at multiples of ω_m. The contribution to the time evolution comes only from the terms that are on resonance with the laser frequency. Writing the Hamiltonian for an interaction between $|g,n\rangle$ and $|e,m\rangle$ in the interaction representation :

$$H = \frac{\hbar\Omega_{m,n}}{2}\hat{\sigma}^{+}e^{-i(\phi+\delta t)}|m\rangle\langle n| + h.c$$

with $\Omega_{nm} = \Omega e^{-\frac{\eta^2}{2}}\eta^{m-n}\left(\frac{n!}{m!}\right)L_n^{m-n}$; $(m \geq n)$ is the generalized Rabi frequency (L_n^{m-n} is the closed form of the Laguerre polynomials), and $\delta \equiv \omega_L - \omega_0 - (m-n)\nu$.

In this Hamiltonian, all transitions can occur. But, in the Lamb-Dicke regime, the transitions amplitude scales as increasing power of η, whereas the second sidebands of the order η^2 are suppressed. Thus, we can understand three kinds of transitions that depend on the effective state that are on resonance: Carrier (n,n) - Does not change the vibrational state, red sideband (RBS: $n, n-1$) removes one quanta of motion following absorption, and blue sideband (BSB: $n, n+1$) that adds one quanta of motion due to emission. The effective Rabi frequency depends on the harmonic state. By measuring the population oscillations under this Hamiltonian and using Fourier transform, one can extract the harmonic state population. These resonances are observed by scanning the laser detuning δ and measuring the population. From equation (1) we can calculate the overlap between the displaced initial harmonic oscillator wave-function and some final harmonic oscillator wave-function, known as the Debye-Waller factor:

$$\begin{cases} \langle D, m \left| H_{int} \right| S, n \rangle = \frac{\Omega_{m,n}}{2} e^{-i(\delta-(n-m)\nu t)} D_{n.m} \\ D_{n,m} = \left\langle m \left| e^{i\eta\left(\hat{a}+\hat{a}^{\dagger}\right)} \right| n \right\rangle = e^{-\frac{\eta^2}{2}} \left(\frac{min(n,m)!}{max(n,m)!}\right)^{1/2} \eta^{|n-m|} L_{min(n,m)}^{|n-m|}\left(\eta^2\right) \end{cases}$$

where L_{min}^{α} is the modified Laguerre polynomial. In the Lamb-Dicke regime we obtain:

$$\begin{cases} D_{Carrier} & = 1 - \eta^2 \left(n + \frac{1}{2}\right) \\ D_{RSB} & = i\sqrt{n}\eta \\ D_{BSB} & = i\sqrt{n+1}\eta \end{cases}$$

From here the dependence of the Rabi frequency will be: $\Omega_{n,n} = \Omega\left(1 - \eta^2\left(n + \frac{1}{2}\right)\right)$. Note that the coupling for the RBS vanishes on $n = 0$ but will always be finite for BSB.

2.3.2 Gates

To coherently control the state of n qubits, we need to apply the basic operations of quantum computing known as quantum gates. A quantum gate over a set of n qubits is described by a $2^n \times 2^n$ unitary matrix U. To allow coherent control of a quantum state, one needs to have the ability to connect any two-state vectors in the Hilbert space. This operator can be approximated by concatenating a finite number of operators chosen from a small set that is called a universal gate set. A sufficient gate set for universal quantum computing consists of arbitrary single qubit rotations and a single entangling quantum gate [24]. In the experiment that we have conducted in order to test the live readout performance, we used several quantum gates that together consist of a universal gate-set. All of them involve interaction with laser beams. The advantage of using laser-ion interaction comes from the fact that even closely spaced ions can be still individually addressed [3, 25].

Single qubit rotation gates:

Single unitary qubit operation can be described as a rotation of the Bloch vector on the Bloch sphere $R(\beta, \phi, \theta)$. Here, β, ϕ determine the direction on the axis around the Bloch vector is rotated: $\hat{\mathbf{n}} = (cos\beta cos\phi, cos\beta sin\phi, sin\beta)$. θ is the rotation angle. All single qubit rotations are a 2×2 unitary matrices with a unity determinant [26]. This is also known as the $SU(2)$ representation group; thus,

the generators of this group are the four Pauli matrices: $\mathbb{1}, \hat{\sigma}_x, \hat{\sigma}_y, \hat{\sigma}_z$ making the rotation operator:

$$R(\beta,\phi,\theta) = R(\hat{\mathbf{n}},\theta) = e^{-i\hat{\sigma}\cdot n\frac{\theta}{2}} = \begin{pmatrix} cos\frac{\theta}{2} - in_z sin\frac{\theta}{2} & -(in_x + n_y)\, sin\frac{\theta}{2} \\ (-in_x + n_y)\, sin\frac{\theta}{2} & cos\frac{\theta}{2} + in_z sin\frac{\theta}{2} \end{pmatrix}$$

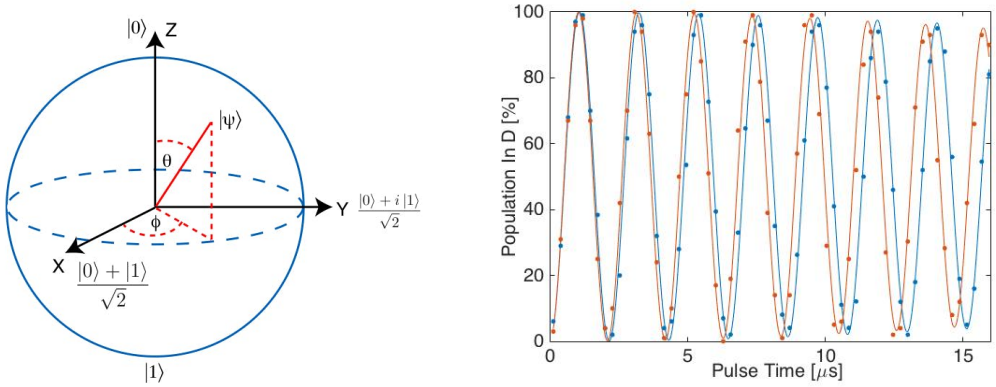

Figure 1: **The Bloch sphere and Rabi Oscillations**. **Left**: The Bloch sphere is a geometrical representation of a pure state space of a two-level quantum system. The eigenbasis of the free Hamiltonian is usually detonated in the $\hat{z}$ direction (marked as $|0\rangle$). The angle θ is the angle between the state vector and $|0\rangle$ .The angle ϕ represents the angle between the $\hat{x}$ axis ($\frac{|0\rangle+|1\rangle}{\sqrt{2}}$ in the drawing) and the projection of the state vector on the equator of the Bloch sphere. **Right**: Rabi oscillations of two ions between the $5S_{\frac{1}{2}}$ and the $4D_{\frac{5}{2}}$. The Rabi time is 1.07 μs and 1.05 μs and the fit corresponds to $\bar{n} = 7.3$ *and* 7.8.

The implementation of a single qubit rotation is done on the optical qubit using the 674 nm laser that couples to the $5S_{\frac{1}{2}} \leftrightarrow 5D_{\frac{5}{2}}$ transition. The control over the rotation angle θ is determined by the duration and amplitude of the pulse and the rotation axis controlled by the phase. An example for a highly used qubit rotation is the Hadamard gate which rotates the qubit axes to be 45° between the $Z - X$ axis. This gate is written as:

$$H = \begin{pmatrix} 1 & 1 \\ 1 & -1 \end{pmatrix}$$

Operating this gate on a qubit will change the qubit bases from $|S\rangle, |D\rangle$(our

representation of $|0\rangle, |1\rangle = |S\rangle, |D\rangle$), to the x basis represented by $|+\backslash-\rangle$:

$$|+\rangle = \frac{|S\rangle + |D\rangle}{\sqrt{2}}$$
$$|-\rangle = \frac{|S\rangle - |D\rangle}{\sqrt{2}}$$

Two optical qubit gates:

The standard universal gate set includes two main gates: single-qubit rotations and CNOT entangling operations. A CNOT gate rotates the state of a target qubit around the x-axis by 180° depends on the logical state of the control qubit. When starting from two qubits at the ground state $|\psi\rangle = |S\rangle |S\rangle$, a CNOT will generate an entangled pair - a Bell state:

$$|\psi\rangle = \frac{|SS\rangle + |DD\rangle}{\sqrt{2}}$$

The original proposal to generate a universal two-qubit entangling gate in trapped ions systems using the interaction of the internal state coupled to the collective motion was initially suggested by Cirac and Zoller [4]. Since then, the implementation of entangling gates on trapped ions is usually done using a Mølmer-Sørensen (MS) gate [27]. This gate is equivalent, by a single qubit rotations, to a CNOT gate discussed above. In this method, entangling ions is done by addressing their harmonic trap degrees of freedom, regardless of their initial state (as long as they are in the Lamb-Dicke regime), meaning there is no need for cooling to the ground state. The MS entangling gate operates on the initial state $|\psi_{initial}\rangle = |SS, n\rangle$. Following [27], the system Hamiltonian is:

$$\hat{H} = \hat{H}_0 + \hat{H}_{int}$$

Where:

$$\begin{cases} \hat{H}_0 = \hbar\omega_0 \sum_i \frac{\sigma_z^{(i)}}{2} + \hbar\nu \left(\hat{a}^\dagger \hat{a} + \frac{1}{2}\right) \\ \hat{H}_{int} = \sum_i \frac{\Omega}{2} \sigma_i^+ e^{i\eta\left(\left(\hat{a}+\hat{a}^\dagger\right) - \omega_L t\right)} + h.c. \end{cases}$$

where ν is the trap frequency, $\hbar\omega_0$ is the energy difference between the ground and the excited state (S and D). ω_L and Ω are the frequency and Rabi frequency of the laser addressing ions, η is the Lamb-Dicke parameter, and $\hat{a}$, $\hat{a}^\dagger$ are the harmonic trap annihilation and creation operators. Moving to the interaction picture with respect to $\hat{H}_0$ and after applying the RWA by assuming $\Omega \ll \nu$ we obtain the interaction Hamiltonian [28]:

$$\hat{H}_{int} = \hbar\Omega \cdot \left(e^{i\delta t} + e^{-i\delta t}\right) e^{i\eta\left(\hat{a}e^{-i\nu t} + \hat{a}^{\dagger}e^{i\nu t}\right)} \sum_{i} \sigma_i^{+} + h.c.$$

This Hamiltonian can be approximated in the Lamb-Dicke regime by:

$$\hat{H}_{int}\left(t\right) = -\hbar\eta\Omega\left(\hat{a}e^{i\xi t} + a^{\dagger}e^{-i\xi t}\right)\hat{J}_y$$

here, $\xi = \nu - \delta$ denotes the laser detuning from the motional sidebands, and we define $\hat{J}_y$ as the global spin operator:

$$\hat{J}_y = \frac{\sigma_{(1)}^{y} \otimes \mathbb{1}_{(2)} + \mathbb{1}_{(1)} \otimes \sigma_{(2)}^{y}}{2}$$

The propagator for the interaction Hamiltonian is represented by the unitary operator [27]:

$$\hat{U}\left(t;0\right) = e^{-i\frac{\eta^2\Omega^2}{\xi}\left(t - \frac{\sin(2\xi t)}{2\xi}\right)\hat{J}_y^2}\hat{D}\left(\alpha(t)\hat{J}_y\right)$$

Where $\alpha(t) = \frac{\eta\Omega}{\xi}\left(e^{i\xi t} - 1\right)$ and $\hat{D}\left(\alpha\right) = e^{\alpha\hat{a}^{\dagger} + a^{*}\hat{a}}$ is the displacement operator, constitute a spin dependent force (See [28]).

At a time $t = \frac{2\pi}{\xi}$ and $\xi = \frac{2\eta}{\Omega}$, $\hat{U}$ will become $\hat{U} = e^{i\frac{\pi}{2}\hat{J}_y^2}$. This means that $\hat{J}_y^2$ acts as a correlated rotation in the qubit subspace. Such that we get a rotation between the product state and a fully entangled state:

$$\left|SS\right\rangle \rightarrow \frac{e^{i\frac{\pi}{4}}\left(\left|SS\right\rangle + i\left|DD\right\rangle\right)}{\sqrt{2}}$$

This state generated by constructive interference on the even parity, while destructive interference suppresses the amplitudes of the odd parity state $\left|SD\right\rangle, \left|DS\right\rangle$. This is achieved by the dependent force that derives the ions, tuning this force magnitude will set the phase difference. This phase is a geometric phase that each of the ions accumulate by traveling different paths through space. Practically, it generates conditional displacement in phase space by application of bichromatic field to the ions, using the 674 nm laser beam, which is red and blue detuned, close to one of the ion crystal motional mode frequency thus the rest of the modes are negligible. The relative phase between the frequencies will determine the phase of the gate.

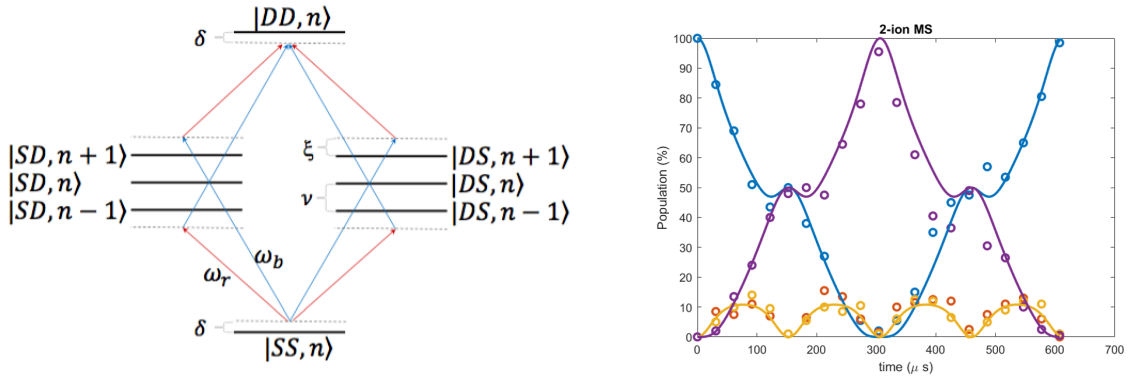

Figure 2: **Mølmer-Sørensen gate operation diagram**. **Left** (adapted from figure 2 in [29]): the bichromatic laser beam interacting with the internal state of the two qubits represented as $|SS\rangle, |DD\rangle, |SD\rangle, |DS\rangle$, superimposed with the harmonic trap levels $|n\rangle$. Here the blue detuned beam $\omega_b = \omega + \nu + \xi + \delta$ and red detuned beam $\omega_r = \omega - \nu - \xi + \delta$ where ω is the $|S\rangle \leftrightarrow |D\rangle$ frequency, ν- trap frequency, ξ, δ is the symmetric\anti symmetric detuning. In the symmetric detuning, an amount of ξ is added to the blue sideband and subtracted from the red sideband making their sum to cancel. The anti-symmetric detuning is the detuning of the frequencies sum from the two-photon transition. MS gate can be interpreted as an excitation of the qubit state while annihilating (ω_r) or creating (ω_b) a harmonic trap phonon. **Right**: A Mølmer-Sørensen population evolution executed using two trapped ions in a Paul trap in our lab for a period of 2π. The $|SS\rangle$ and $|DD\rangle$ population (blue and purple) are at 50% ,and the SD and DS are at 0, making it a valid entangling gate.

3 Experimental Setup

3.1 The system

The strong interaction between an electric field and an electric charge allows the implementation of very deep and tightly confined $3d$ charged particle traps that provide long trapping times. The Paul trap initially designed by Wolfgang Paul (for which he shared the 1989 physics Nobel prize (together with Dehmelt and Ramsey)) as a mass filter was soon after modified to allow the confinement of particles in all directions. The Paul trap uses a fast oscillating electric field in order to create a $3d$ harmonic pseudo-potential to trap single or few ions that can be used as a platform for spectroscopy, precision measurements, quantum optics and quantum information. Our experimental set up contains a Paul trap, lasers used to ionize ^{88}Sr atoms, Doppler cool, initialize, measure, excite\de-excite, and repump them. Here is a brief overview of the system. Extensive details regarding the ion trap, lasers, optical paths, and electronics are discussed in [30, 31, 25]

3.1.1 Ion Trap

The ions are trapped in a linear Paul trap. Our trap has four parallel conducting tungsten electrodes that are placed in a quadrupole configuration, where two opposite diagonal electrodes are held in a constant voltage, and the other two conduct oscillating voltage at $21MHz$ that is responsible for the confinement in the radial axis. Between the four electrodes, there are two end-caps (tungsten rods), one on each side that are held at a constant voltage to allow for axial confinement. Below the trap, two more electrodes are placed. One is used to drive the RF magnetic field in the direction of the RF electrodes. This is used to drive transitions in the ion's internal level structure. The second one is to compensate for stray electric fields in the RF electrodes direction.

The six electrodes create a (nearly) harmonic pseudo-potential. The trap spring constant and frequencies determine the confinement of the ions. The trap frequencies are $2MHz$ in the radial direction and $1MHz$ in the axial direction.

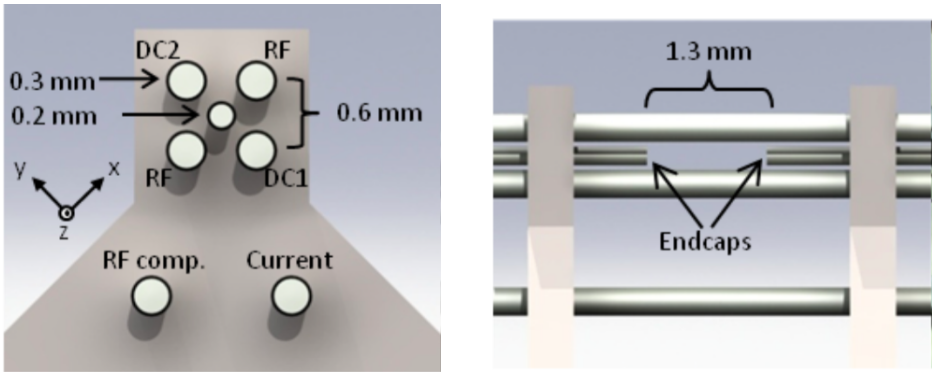

Figure 3: **The Paul trap in our lab** (adapted from fig 1.3 of [30]) The two $0.2mm$ end-caps rods create the trapping potential in the axial direction (typically $\sim 1.5MHz$), separated by $1.3mm$ which consists the trapping region of the ions. The four $0.3mm$ rods held in a $0.6mm$ square are the RF and DC electrodes that create effective harmonic potential in the radial plane (typically $\sim 2.5MHz$), which is the fast oscillating quadrupole potential.

3.1.2 Vacuum chamberfield, has motivated work towards optimizing QEC methods. Although

The Paul trap is placed in a vacuum chamber, which maintains an ultra-high vacuum of about 10^{-11} $Torr$. This is crucial for preventing collisions of room-temperature molecules with the ion chain that can cause chemical reactions of the Strontium ions with the background gas and lead to loss of ions from the trap or change in their chemical identity. Moreover, it can cause heating.

3.1.3 $^{88}Sr^{+}$ as a qubit

Quantum information is encoded in the internal electron levels of the trapped ions. Ions with a single electron in the valance shell are relativity simple, thus suited for this purpose. Strontium is an alkaline earth metal (2nd row in the periodic table). Thus it has two electrons in the valance shell. Also, it is heavy enough to have a D orbital in the $(n-1)$ shell. Stripping one electron leaves the $^{88}Sr^{+}$ with a single electron in the valance shell and a Hydrogen-like level structure. The different states of the ion are denoted by: Angular momentum $L \in \{S, P, D...\}$; Total angular momentum $J \in \{\frac{1}{2}, \frac{3}{5}, \frac{5}{2}\}$, and the projection on the z-axis of the total angular momentum $m \in \{0, \pm\frac{1}{2}, \pm\frac{3}{5}, \pm\frac{5}{2}\}$. The ground state is given by $5S_{\frac{1}{2}}$ state, which can split into two Zeeman states with magnetic susceptibility of $2.802[\frac{MHz}{Gauss}]$. The next lowest excited state (besides the meta-stable state) is the $5P_{\frac{1}{2}}$ state, which is dipole coupled to the ground state, this results in a

short lifetime of $\sim 8ns$. $^{88}Sr^{+}$ also has the $4d^2D_{\frac{3}{2}}$ and the $4d^2D_{\frac{5}{2}}$ fine-structure levels that are between the $S \rightarrow P$ levels. Both S and D orbitals have even parity making the electric dipole transition forbidden, so an electric quadrupole transition couples them. This means that the D orbital has a relatively long lifetime ($0.38s$ for the $4D_{\frac{5}{2}}$ before it decays back to the ground state); hence the natural width of the $5S_{\frac{1}{2}} \leftrightarrow 4D_{\frac{5}{2}}$ transition is narrow.

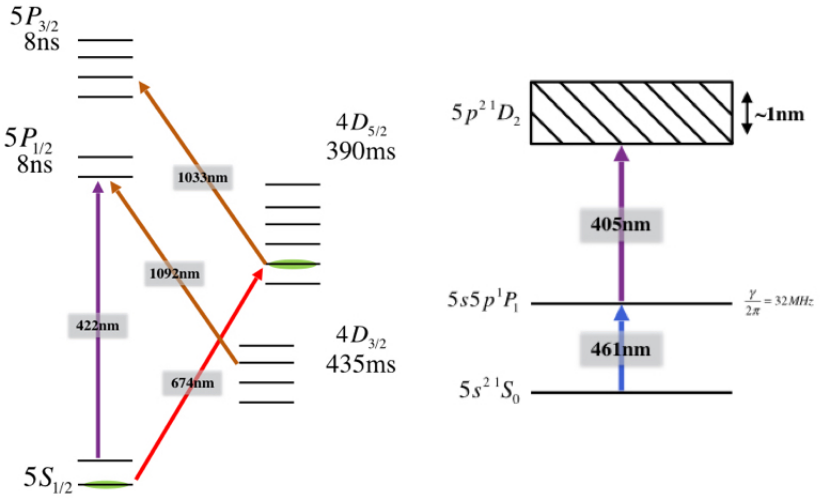

Figure 4: **Energy levels** of $^{88}Sr^{+}$ ion with the lasers used in the lab. (adapted from fig 2.1 and 2.2 in [30]). **Left:** Energy level of $^{88}Sr^{+}$ ion, lifetime, and lasers available in the setup. The 422 nm laser couples the dipole transition to the short-lived $5P_{\frac{1}{2}}$ manifold ($8\,ns$). This transition is used for detection, Doppler cooling, state preparation, and EIT cooling. The 674 nm narrow laser couples one level of the $5S_{\frac{1}{2}}$ manifold to one of the $4D_{\frac{5}{2}}$levels through a quadrupole transition. This transition is used as the optical qubit (marked in green) due to the long lifetime of the $4D_{\frac{5}{2}}$ manifold ($390\,ms$) , relative to the Rabi time ($\sim 2.8\mu s$). In order to pump the system to the ground state a $1033\,nm$ laser repump the $4D_{\frac{2}{5}}$ to the $5P_{\frac{3}{2}}$ short-lived ($8\,ns$) manifold, and from there, the electron will decay back to the ground state. The $1092\,nm$ laser repump the $4D_{\frac{3}{2}}$ manifold to the $5P_{\frac{1}{2}}$. This is done because there is a branching ratio of $\sim 1:16$ from the $5P_{\frac{1}{2}} \rightarrow 4D_{\frac{3}{2}}$. **Right:** Ionization scheme - the ionization is done using a two-photon transition. First, a $461\,nm$ laser beam excites one electron from the $5s^{21}S_0$ manifold to the $5s5p^1P_1$ level (from S orbital to 5P orbital). Then, a 405 nm laser excites the second valence electron, and then through an Auger process, one of the excited electrons decays back to the ground state, and the other ionizes the atom.

In our system we are working with two kinds of qubits - The first is Zeeman ground state qubit where the transition between the states is driven via RF field and the second is the $5S_{\frac{1}{2}} \rightarrow 4D_{\frac{5}{2}}$ qubit where the transition is optical and driven by the 674 nm laser. The Zeeman and optical qubits are both initialized using optical pumping with the 422 nm or the 674 nm lasers. For the Zeeman qubit,

the polarization of the laser set to be circular σ^+. This polarization corresponds to one of the Zeeman levels that can be excited to the $5P_{\frac{1}{2}}$ state, and from there, it can spontaneously decay back to the ground state. The ion will end up in a dark spin state that is uncoupled from the fluorescence cycle due to angular momentum conservation. In the latter case, the narrow 674 nm quadrupole transition is used to excite the population of one of the Zeeman states to the $5D_{\frac{5}{2}}$ state, and from there the population is pumped using the 1033 nm laser to the $5P_{\frac{3}{2}}$ then it will spontaneously decay to the both of the $5S_{\frac{1}{2}}$ levels. Eventually, the ion will end up in a spin state that is uncoupled from this cycle - a dark state. In both types of qubits, detection is done using *state-selective fluorescence* using the 422 nm fluorescence on the $5S_{\frac{1}{2}} \leftrightarrow 5P_{\frac{1}{2}}$ transition: in both cases, we will use the optical transition to detect. In the optical qubit, if the qubit collapses to the $5S_{\frac{1}{2}}$ state, this means that the ion fluorescence via the $5S_{\frac{1}{2}} \leftrightarrow 5P_{\frac{1}{2}}$ transition, emit photons that can be collected and detected. If the qubit collapses to the $4D_{\frac{5}{2}}$ state, the $5S_{\frac{1}{2}} \leftrightarrow 5P_{\frac{1}{2}}$ transition is not driven, and no photons will be emitted, scattered, or detected. The detection time is more than two orders of magnitude shorter than the D level lifetime. Thus, spontaneous decay to the ground state from the D level has a small effect on the detection fidelity.

For the Zeeman qubit, the qubit state mapped onto the optical qubit using the 674 nm narrow quadrupole transition from one of the Zeeman states to the $4D_{\frac{5}{2}}$ state and from there using the same detection scheme as with optical qubit.

Taking into consideration the $4D_{\frac{3}{2}}$ level and the $5P_{\frac{3}{2}}$ level means that we need two more "repump" lasers. The 1092 nm laser that corresponds to the $4D_{\frac{3}{2}} \leftrightarrow 5P_{\frac{1}{2}}$ transition, is required to maintain fluorescence from the ion due to the fact that while excited to the $5P_{\frac{1}{2}}$ level the ion can spontaneously decay not just to the $5S_{\frac{1}{2}}$ level and but also with a $\frac{1}{16}$ probability to the $4D_{\frac{3}{2}}$ level, then fluorescence will stop for, on average, 380 ms - the lifetime of that level. The 1092 nm thus re-excites the ion to the $5P_{\frac{1}{2}}$for continued fluorescence. The 1033 nm laser is tuned to the $4D_{\frac{5}{2}} \leftrightarrow 5P_{\frac{3}{2}}$ transition in order to allow re-initialization to the ground state without waiting for spontaneous decay from the long-lived level - usually after the detection cycle is completed. Errors in state selective fluorescence will be mostly due to initialization errors, shelving errors, laser scattering in the dark state, and the fact that the $D_{\frac{5}{2}}$ has a finite lifetime [32]: Initialization error sources are imperfect polarization of the optical pumping light due to polarizer quality and stress-induced birefringence on the vacuum chamber window, and a possible misalignment of the optical pumping light with respect to the magnetic field. Shelving error sources are laser intensity fluctuations of the 674 nm laser, thermal occupation of the harmonic oscillator levels (heating of the ions), frequency drifts,

and off-resonance coupling. Scattering in the dark state is mainly due to the scattering of the laser beam from the trap surfaces. Finally, in the case of optical qubit, the finite lifetime of the $D_{\frac{5}{2}}$ puts an upper bound to the time quantum information can be stored . Moreover, it will cause the distribution functions of the bright and dark states overlap to increase over the detection time due to the growing tail of the dark state distribution (see section 4 in [32]). This fact can harm the discrimination efficiency, making the need to find and optimize the threshold and the detection time used in our experiments.

3.1.4 Lasers

In order to ionize, cool, manipulate the ions, we use six different lasers: two for photo-ionization, two "repump" lasers, the 422 nm laser for detection, optical pumping, and Doppler cooling and the 674 nm which is used for qubit manipulation and optical pumping.

422 nm - detection, optical pumping, electromagnetically induced transparency cooling:

The 422 nm laser is generated by an 844 nm external-cavity diode laser (ECDL) coupled to a butterfly cavity with a nonlinear crystal (BBO) as a frequency doubler. The emission of the 844 nm laser is locked using the Pound-Drever-Hall (PDH) technique to an external cavity to give the laser short-term frequency stability. The cavity length can be tuned using a piezo-electric transducer (PZT). The cavity length is then locked by a saturation-absorption method to a ^{85}Rb resonance using a vapor cell. Serendipitous, this convenient atomic resonance is of 440 MHz red-detuned from the Strontium wanted transition. In order to mitigate this difference and generate both a far-detuned off-resonance cooling beam (360 MHz), an on-resonance beam for detection, optical pumping, and near-resonance cooling, we are using two double-pass AOMs.

Optical pumping

Is used for state preparation. This is done by shining on the ions circular polarized light (parallel to the magnetic field axis which splits the $S_{\frac{1}{2},\pm\frac{1}{2}}$ level). The polarized light only couples one of the $S_{\pm\frac{1}{2}}$ levels, for example σ^+polarized light only couples to the $5S_{\frac{1}{2},-\frac{1}{2}} \rightarrow 5P_{\frac{1}{2},\frac{1}{2}}$ - meaning that the $+\frac{1}{2}$ spin-state is a dark state. From here the electron will decay quickly to both of the S levels, but the remaining population in the $S_{\frac{1}{2},-\frac{1}{2}}$will be excited again. The probability of

measuring the ion in the $S_{\frac{1}{2},-\frac{1}{2}}$ after n cycles is $\frac{1}{2^n}$, which means that the state optically pumped to the $S_{\frac{1}{2},\frac{1}{2}}$ state.

Doppler cooling

Is implemented using a red-detuned (lower frequency) $422\,nm$ beam with a frequency of $\omega_{422} = \omega_0 - \delta$. When the ions in the trap have a velocity of v towards the laser beam's $k's$ vector, the frequency in the ion frame of reference is changed by $\Delta\omega(v) = k \cdot v$ due to the Doppler effect. The laser detuning is set to be $\delta \sim \Delta\omega(v)$ which means that now the laser is closer to resonance when the ion is oscillating towards the laser beam (i.e., has a velocity component projected opposite to the laser k-vector) and can excite it to $5P_{\frac{1}{2}}$, in this case, the absorbed photon will have a momentum of $-\hbar k$ that will slightly slow down the ion. The fact that the emission of photons from the ions (when decay back to $5S_{\frac{1}{2}}$) is in a random direction means that the average momentum given to the ion in the emission process is zero. Notice that the average k^2; i.e., kinetic energy, given to the ion in the emission does not null. Instead, it diffuses and increases as the square of the number of photons emitted. This heating mechanism limits the Doppler cooling method to a minimal temperature of $T_{Doppler} = \frac{\hbar\gamma}{2k_B} \approx 0.5mK$ $\left[\gamma \text{ is the decay rate from } 5S_{\frac{1}{2}} \rightarrow 5P_{\frac{1}{2}}\right]$. To get below this temperature limit, we are using resolved sideband ground-state cooling, and recently added EIT cooling.

Ground state cooling

The Doppler cooling limit is not sufficient to maintain high fidelity qubit operations. High fidelity operations requires $\bar{n}$ to be close to the ground state. Cooling to the ground state is achieved by applying resolved sideband cooling on the narrow quadrupole transition (the transition linewidth needs to be narrower than the motional mode frequency of the mode that is cooled). The cooling is done by tuning the laser frequency to the red motional sideband of the mode to be cooled. The ion is brought from the electronic ground state $\left|S_{\frac{1}{2}}, n\right\rangle$ to the excited state in the $\left|D_{\frac{5}{2}}, n-1\right\rangle$ manifold while the number of motional excitations is reduced be one. The 1033 nm repump laser, quenches back the electron to the ground state via the $P_{\frac{3}{2}}$ excited state followed by spontaneous emission. This cycle is repeated until the ion population has been pumped to the dark state of the red sideband excitation, which is the ground state. For more information, see chapter 3.4 in [30].

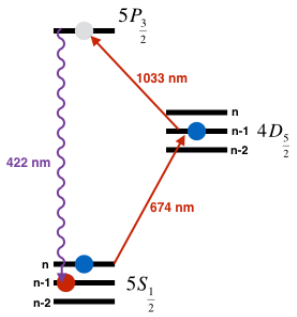

Figure 5: **Sideband cooling on the qubit transition**. The motional states are marked with n. The slightly red-detuned 674 nm laser excites the electron state from $\left|5S_{\frac{1}{2}}, n\right\rangle$ to $\left|4D_{\frac{5}{2}}, n-1\right\rangle$, using the 1033 nm laser the electron will decay back to $\left|5S_{\frac{1}{2}}, n-1\right\rangle$ via the $5P_{\frac{3}{2}}$ level.

Electromagnetically induced transparency (EIT) cooling

A ground state cooling technique for trapped particles by cooling all the motional modes at once. EIT cooling requires a three-level Λ systems where the coupling of the two ground states, $|g\rangle, |r\rangle$ to one short-lived excited state $|e\rangle$ will lead to coherent population trapping in a superposition of the two ground states that does not couple to the excited state [33]. The $|g\rangle \rightarrow |e\rangle$ transition is driven with a Rabi frequency Ω_σ, with a blue detuned by Δ laser beam. This field dressed the ground and excited states which are light shifted up-wards or downward in frequency from the bare states with an amount of

$$\delta = \frac{1}{2}\left(\sqrt{\Omega_\sigma^2 + \Delta^2} - |\Delta|\right)$$

A probe beam drives the $|r\rangle \rightleftarrows |e\rangle$ transition with detuning Δ_π and a Rabi frequency $\Omega_\pi \ll \Omega_\sigma$. The coupling of the second ground state to the dressed state creates a Fano-like absorption. Usually, this absorption goes to 0 when $\Delta_\pi = \Delta$. However, since the ions are trapped in a harmonic trap with frequency ω, it absorbs light from the vibrational sidebands of the transition (instead of zeroing out). If the light shift $\delta = \omega$, the absorption probability on the red sideband transition $|r, n\rangle \leftrightarrow |g, n-1\rangle$ maximize. This results in a decrease of the phonon number n by one unit for every absorption event, which leads to cooling. On the other hand, the only heating mechanism is due to blue sideband absorption, which is much smaller than the red sideband absorption.

A differential equation describes the cooling process dynamics for the mean phonon number $\bar{n}$:

$$\dot{\bar{n}} = -\eta^2 \left(A_- - A_+\right) \bar{n} + \eta^2 A_+$$

here, $\eta = |(\mathbf{k}_\pi - \mathbf{k}_\sigma) \cdot \mathbf{e}_m| \sqrt{\frac{\hbar}{2m\omega}}$ is the Lamb-Dicke factor with wave vector $\mathbf{k}_\sigma$ for the dressing probe, and $\mathbf{e}_m$ is the unit vector describing the oscillation direction of the mode to be cooled. $A_\pm$ is the rate coefficients:

$$A_\pm = \frac{\Omega_\pi^2}{\Gamma} \frac{\Gamma^2 \omega^2}{\Gamma^2 \omega^2 + 4\left(\frac{\Omega_\sigma^2}{4} - \omega\left(\omega \mp \Delta\right)\right)^2}$$

with Γ as the linewidth of the transition. The steady state solution of the dynamics equation is:

$$\langle \bar{n} \rangle = \frac{A_+}{A_- + A_+}$$

and the cooling rate is :

$$R = \eta^2 \left(A_- - A_+\right)$$

In Sr^+, the three-level system discussed above can be approximated by using the Zeeman sub levels of the $S_{\frac{1}{2}} \leftrightarrow P_{\frac{1}{2}}$ dipole transition at $422\ nm$. The relevant energy levels of Sr^+ are shown in figure 6. The dressed states are generated by the σ_+ laser beam that is parallel to the optical pumping beam, that couples the $\left|S_{\frac{1}{2},-\frac{1}{2}}\right\rangle$ ground state to the $\left|P_{\frac{1}{2},\frac{1}{2}}\right\rangle$ excited state. The π polarized beam (parallel to the off-resonance cooling beam) couples the $\left|S_{\frac{1}{2},\frac{1}{2}}\right\rangle$ to $\left|P_{\frac{1}{2},\frac{1}{2}}\right\rangle$. The configuration of the beams are such, so the subtraction of the beams $\mathbf{k}$ vectors will be in the direction of the modes that we are interested in cooling. The detuning of the dressing beam set to be around $60\,MHz$ from resonance of the $S \leftrightarrow P$ transition [34, 35].

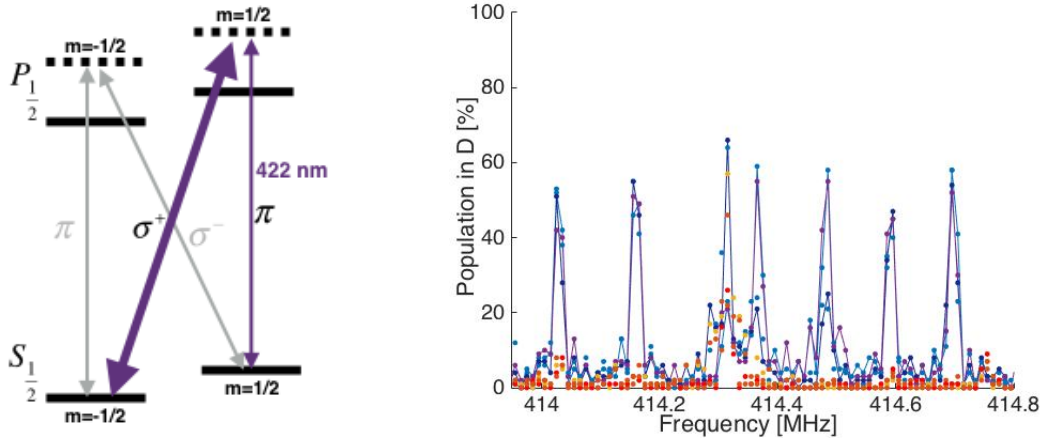

Figure 6: **EIT cooling**. **Left**: scheme of the Sr^+ transition used for EIT cooling. **Right**: EIT cooling of the radial sidebands in a four ions chain. There are eight radial sidebands (two are missing from the image) and one axial sideband. The cool colors are the sideband without EIT cooling, where the warm colors are with EIT cooling. The one sideband that remained is the highest energy axial mode that is not cooled in the scheme that we are working with.

Detection

State selective fluorescence processes is done using the transition induced by the 422 nm laser. The signal from the ions is used to detect the ions and to distinguish between their internal state with high detection efficiency [36]. More information about the detection processes is in section 3.3.

674 nm - qubit manipulations

The 674 nm laser couples the $5S_{\frac{1}{2}} \rightarrow 4D_{\frac{5}{2}}$ manifolds through a quadrupole transition and is used for coherent manipulation of the optical qubit. This is an extremely narrow linewidth laser (FMHW $\sim 20\,Hz$), used to selectively address the desired Zeeman states in the S and D manifolds and preform coherent manipulation on this optical transition. To achieve this narrow linewidth, the laser is locked twice using PDH schemes in series with high-finesse cavities. The light is generated by an ECDL which is locked to a high-finesse cavity ($f = 86000$) by a PDH scheme using current modulation. After the first locking circuit, the cavity transmits $\sim 200\mu W$. The first cavity acts also as a good filter for high frequency phase-noise that is introduced by the servo loop. To amplify the optical power of the stable light after the cavity, the light is injected into a slave diode that optically locks its frequency. This light passes through an AOM and a portion of it is taken to the second high-finesse cavity ($f = 500,000$). The 2nd cavity error signal modulates the AOM and corrects the frequency which provides a short term stability of

$\sim 20MHz$ [31] (although the cavity drifts on the order of kHz a day). After the laser is locked and stabilized, a portion of it goes to the individual addressing line, and the rest is injected into a second slave diode, outputs $15mW$ that goes into a tapered amplifier with a $670nm$ center gain frequency. The tapered amplifier amplifies the injected light to about $180mW$. The light then goes through a double pass ($160 \cdot 2\,MHz$) AOM and a single pass AOM ($80\ MHz$) that controls the frequency of the laser (they also acts as a switch of the $674\,nm$ light into the trap). At the end of the line, the light is coupled to a single-mode fiber that exits next to the trap with about $10\ mW$ of power, resulting in a Rabi π time of $1\,\mu s$ on the carrier transition. This is orders of magnitude faster than the D manifold decoherence time of milliseconds, meaning that many operations can be executed before the ion will de-phase (it is actually limited by the magnetic noise decoherence time).

461 nm and 405 nm - ionization lasers

In order to photo-ionize the neutral Strontium atom, we use a resonant two-photon ionization process with two independent lasers (see 4). First, using a 461 nm laser that is generated using a $2nd$ harmonic generation process from a 921 nm ECDL coupled to a nonlinear crystal. Then with a 405 nm laser generated by a diode.

1033 nm and 1092 nm - repump lasers

The 1092 nm repump laser is generated by an ECDL, which is locked to a Febry-Pèrot cavity using a PDH method. The 1033 nm laser is generated by an ECDL and locked to the same cavity.

3.2 Imaging system

The ions are optically imaged using a 422 nm fluorescence through a 0.34 numerical aperture objective onto a fast electron-multiplying charge-coupled device (EMCCD) camera embedded with a Camera Link connector. This imaging system, along with the Camera Link connector, allows high-speed imaging (less than a 1 ms), and simultaneous fast readout ($< 500\mu s$) of the state of several ions. This chapter will discuss the technical details of the imaging system (for a detailed description of the imaging system, refer to [25]) .

3.2.1 Optical Layout

$^{88}Sr^{+}$ ion fluorescence at 422 nm emits $\sim 10^7$ photons per second. The photons are scattered isotropically. The portion of the light, which is directed toward the numerical aperture, is collected by an objective. The objective positioned outside the vacuum chamber and focuses the light onto the Andor iXon Ultra 879 EMCCD camera positioned $\sim 1250mm$ away from the objective. The objective provides a $\times 40$ magnification. A Dove prism set near the camera can adjust the orientation of the ion-crystal image with respect to the EMCCD rows. Since the same imaging system serves both to collect 422 nm fluorescence as well as individually address the ions with 674 nm laser light, spectral filtering of the light reaching the camera is needed. Therefore a dichroic mirror reflects the fluorescence from the 422 nm onto the camera (fitted with a 422 nm filter to clean unwanted background light) while allowing the 674 nm single addressing beam pass through. The fluorescence rate of the ion, simplified to a two-level system, when it is in the $|S\rangle$ ground-state can be calculated as:

$$R = A_{S\leftrightarrow P} \cdot p_{P_{1/2}}$$

where A is the Einstein coefficient for the $S \leftrightarrow P$ transition and $p_{P_{1/2}}$ is the excited state $P_{1/2}$ population. The excited state population can be calculated as the steady-state solution of the optical Bloch equations:

$$p_{P_{1/2}} = \frac{\frac{I}{I_{sat}}}{2\left(1+\frac{I}{I_{sat}}\right)}$$

Where $\frac{I}{I_{sat}}$ is defined as the saturation parameter $\frac{I}{I_{sat}} = s \equiv \frac{2\frac{|\Omega|^2}{\Gamma^2}}{1+4\frac{\delta^2}{\Gamma^2}}$; $2\frac{|\Omega|^2}{\Gamma^2} \equiv s_0$ is the on resonance saturation parameter, and Γ is the spontaneous decay rate between $S \leftrightarrow P$. Plugging back the full expression we get that the population of the excites state is:

$$p_{P_{1/2}} = \frac{\frac{s_0}{2}}{\left(1+\left(\frac{2\delta}{\Gamma}\right)^2+s_0\right)}$$

The objective numeric aperture is 0.34 giving an effective focal length of 30 mm and is built from $1-inch$ diameter lenses making the photon collection efficiency :

$$Collection\ efficiency \approx \frac{\pi R^2}{4\pi f^2}$$

Where $R = \frac{D}{2}$, f is the focal length working distance. Giving $\frac{D}{f} = NA$:

$$Collection\ efficiency = \frac{1}{4}(NA)^2 \sim \frac{1}{36}$$

3.2.2 The camera

We use an Andor iXon Ultra 879 EMCCD [37]. This model has high quantum efficiency (>90%), High sensitivity (up to a single photon sensitivity for some acquisition settings), High readout speed (up to 17 MHz), low temperature thermo-electrically cooling (reduces dark counts in the CCD array), and high gain (×500). The CCD has 512×512 pixels, each pixel is 16×16 μm in size. Taking into account the fact that the point spread function of the imaging system is $1\mu m$ in diameter, the magnification is ×40 and the pixel size - each ion occupies about 2-3 pixels diameter, such that it covers $4 - 10$ pixels on the CCD, meaning a ten ions chain with a physical length of about $\sim 20\,\mu m$ (depends on the trap frequency), will correspond to $\sim 800\mu m$ on the EMCCD, which is about 50 pixels across. The camera is controlled via the PC through a USB 2.0 interface. The communication is done using Matlab with an SDK library with predefined commands for the camera supplied by Andor. The trigger for the camera is controlled by a field-programmable gate array (FPGA) card, which controls the entire experiment and lab equipment.

In a typical experiment, the camera acquisition settings are set by the PC. When the experimental sequence starts, the camera acquisition is triggered by the FPGA, and at the end of that sequence, the data acquired by the camera is read out to the PC through the USB connection, there the data is analyzed offline. The main focus of this thesis is the implementation of a real-time readout system (described in the next chapter) that allows us to access the imaged data during an experiment via Camera Link interface using a dedicated FPGA that interfaces with the FPGA that controls the experiments.

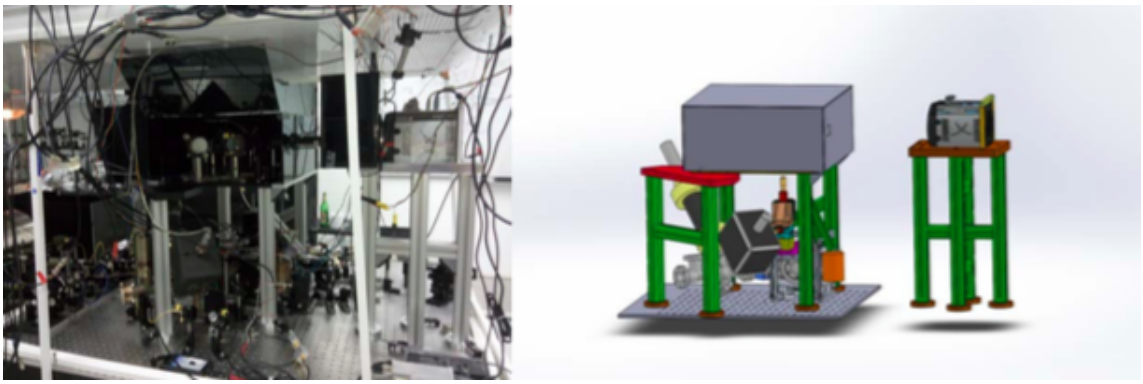

Figure 7: **System mechanical layout** (figures adapted from figure 4.2 in [25]). **Left:** image of the experimental setup. **Right**: A SolidWorks model of the layout

Sensor architecture:

Digital imaging is usually done by a Charged Coupled Device (CCD) - a silicon-based semiconductor chip built out of a two-dimensional matrix light sensitive sensors (pixels) made for capturing images. The sensors contain a photo-active region and a transmission region - a shift register. The imaging process starts when light is projected onto the capacitor array (the photo-active region), causing each capacitor to accumulate an electric charge. The charge is proportional to the light intensity at the capacitor location. The charge is then transferred from each capacitor to its neighbor using a control circuit operating as a shift register. From the last capacitor in the array, the charge is inserted to the charge amplifier, where it is converted into voltages. By repeating this process, the entire contents of the capacitors array is converted to a sequence of voltages that are sampled, digitized, and stored in memory. Electron Multiplying Charged Coupled Device (EMCCD) differs from a conventional CCD by the length of the shift register that is extended to include an additional section - the multiplication (or gain) register (shown in fig 8). This addition comes to make up for the CCD's slow readout time $\sim 1MHz$. The speed limitation arise from the CCD's charge amplifier: High-speed operations require the charge amplifier to have a wide bandwidth. This is a problem because noise scales with the bandwidth. Hence this solution will gain high noise. The multiplication region in an EMCCD amplifies the charge before the charge amplifier hence maintain high sensitivity at high speed, keeping the readout noise by-passed, and no longer limits the sensitivity.

The amplification of charge in the multiplication register occurs in a probabilistic process known as Clock Induced Charge (CIC). CIC utilizes 'impact ionization' - a charge has (with a small probability $p \sim (0.01 - 0.02)$) sufficient energy to create another free electron in the conduction band that creates another one and so on. In an EMCCD the process of impact ionization is feasible because: (a) the electron is initially clocked with higher voltage thus gains more energy and (b) it is designed with hundreds of cells rising the probability for impact ionization and amplification, making the total mean gain $G = (1 + p)^x$ large. Here, x is the number of cells in the gain register.

EMCCD uses a Frame Transfer CCD structure. This structure features two areas - the sensor area, which captures the image and the storage area, which is identical in size to the image area but covered with a foil mask. In the storage area, the image is stored before the readout. During the exposure time, the sensor area is exposed to light, and the charge is accumulating on the sensor. At the end of the exposure time, the charge is automatically shifted downwards to the storage

area and towards the readout register. To readout the sensor, the charge is moved vertically into the readout register and then moves horizontally from the readout register and inserts serially to the output node of the amplifier. This scheme allows short times between exposures but, unfortunately, slows-down the readout because the image is shifted vertically also through the storage area, which adds 512 rows to move through.

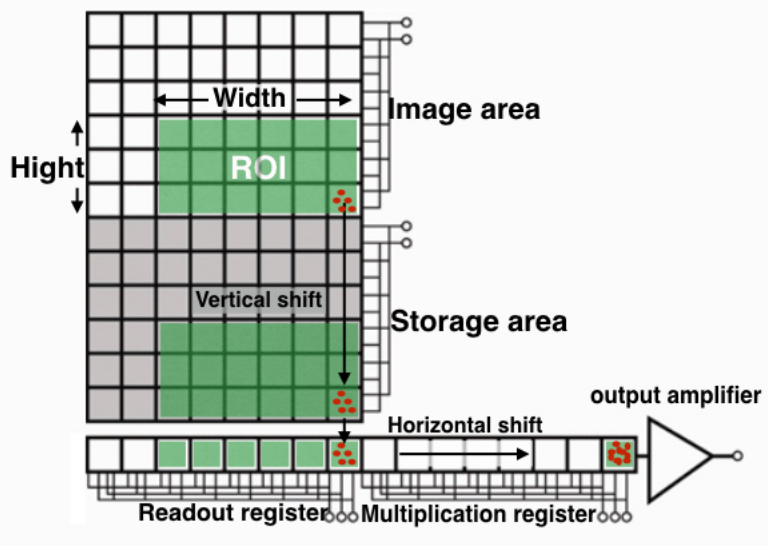

Figure 8: **EMCCD structure.** The image area is a 512×512 pixels, 16 μm each. The ions are located on the bottom right side of the image area. The Region Of Interest (ROI) is usually about $4-5$ rows, and the number of columns change according to the number of ions (for example for a two ions chain the width is about ~ 20 pixels long). The storage area in the Frame Transfer (FT) technology is identical in size to the image area covered with foil and is not exposed to light. After the exposure time, the image (only the ROI) is transferred to the storage area at a rate of $1.6\,MHz$ per pixel. From the storage area, the data is transferred to the readout register and multiplication register, where the pixels are multiplied and transferred to the output amplifier and ADC at a rate of $17\,MHz$ per pixel.

Readout:

Two main parameters control the readout speed of the camera: The horizontal shift speed and the vertical shift speed. Both of these parameters, along with the number of pixels (rows or columns), will set the total readout time. The horizontal shift rate is the time it takes to read one pixel from the shift register. After which it is converted to a "count" at the analog-to-digital converter (ADC). Vertical shift rate is the time it takes to shift one row down towards the shift register, with the bottom row entering the shift register. There is a tread-off when working with fast horizontal and vertical shift speeds: High horizontal shift rates increase the

read noise and reduce the available dynamic range. A disadvantage of fast vertical shift speed, is that the charge transfer efficiency is reduced, and by that reducing the pixel potential well depth. This is mainly a problem for bright signals: if the vertical shift is too fast, some charge may be left behind and will result in a degraded spatial resolution.

The total readout time is calculated immediately after the exposure time until the CCD finishes transferring the pixels in the ROI:

$$t_{readout} = H\left(\bar{W} \cdot t_H + t_V\right) + t_{extra}$$

Here: $\bar{W}$ - image width , H - image height (number of rows), $t_H,\ t_V$−horizontal and vertical shift rates, and $t_{extra} = t_V \cdot H_S + t_H \cdot R$. t_{extra} Takes in account the time delay moving through the storage area and moving through the different registers R. In our camera, the minimum readout time that we have achieved is about $600\mu s$ (data taken from the camera during an experiment). The imaging parameters were: ROI size $5_H \times 20_W$ pixels, with horizontal readout rate of 17 MHz, vertical shift time - $0.3\mu s$, number of registers, R, is 1080, and 48 over-scan pixels.

This time is long because reading out each line includes the shift of a full line width (512 pixels) from the sensor area to the ADC. To solve this problem, the Andor Ixon Ultra has a "Cropped" mode option. In this mode, the camera is fooled to readout only the pixels in a specific region, defined pre-acquisition. This will allow faster readout rates (around 400 μs). In order to work with this mode, we need to ensure that no stray light will fall on pixels outside the cropped mode region. This is done with a mask placed before the camera's EMCCD. For more details about our sensor, see [38, 37].

3.3 State detection

As discussed in 3.1.3, the ions are detected using the 422 nm laser that drives the $5S_{\frac{1}{2}} \leftrightarrow 5P_{\frac{1}{2}}$ transition. When the electron decays back to the ground state due to the short lifetime of the $5P_{\frac{1}{2}}$ level, it emits a photon with the same wavelength. Applying the laser for long enough time ($100's$ of μs) the ion will emit a sufficient number of photons that the camera can collect. When the number of photons is larger than the dark current and within photon shot-noise, the ion will be detected and the state will be recognized as "Bright". The 674 nm laser drives the $5S_{\frac{1}{2}} \leftrightarrow 5D_{\frac{5}{2}}$ transition. Shining the laser for a time corresponds to a full population transition (a π pulse), the electron will be excited from the ground state to the $D_{\frac{5}{2}}$ manifold. Due to the long lifetime of this level (~ 0.5 seconds), when shining the ions with a 422 nm laser while the electron is in the D manifold,

the electron is not coupled to the $5P_{\frac{1}{2}} \leftrightarrow 5S_{\frac{1}{2}}$ transition, and will not emit photons. This state is known as a "Dark" state. The distinction between the two internal ion states is known *as state selective fluorescence detection*. Quantum mechanics has a statistical nature, thus to infer the probabilities of the ion being in each of the two-qubit states with high fidelity, we repeat each experiment a multiple number of times. The next section presents the camera output distribution, detection algorithm, the ability to determine the ion state, and the threshold calculation.

3.3.1 Camera output distribution

In contrast to the incoming photons that follow a Poisson distribution, the EMCCD operation mechanism is complex thus does not follow the same distribution as the incoming photons. The EMCCD output distribution takes into account the probabilistic nature of light - photons Poisson distribution, the response of the imaging system to light, and some noise function. The model described here follows [39, 40, 41]. The charge transfer along the EMCCD can be described by the probability distribution of x electrons at the end of an ideal gain register with gain g, for n incoming photoelectrons. It can be approximated by:

$$p_{n,g}(x) = \frac{\left(\frac{x}{g}\right)^{n-1} e^{-x/g}}{g \cdot (n-1)!}$$

For high gain and low light levels, this distribution mean is $n \cdot g$ and variance $n \cdot g^2$. In high light levels, it can be approximated to a Gaussian (the PSF of the camera for varying exposure times can also describe the charge transfer efficiency of the EMCCD).

The number of photoelectrons on a pixel is drawn from a Poisson distribution, $q_\lambda(n) = \frac{\lambda^n e^{-\lambda}}{n!}$ of incoming photons with mean λ. The distribution of electrons to leave the gain register is a weighted sum over $p_{n,g}(x)$ for the different photoelectrons values:

$$h_{\lambda,g}(x) = \sum_{n=1}^{\infty} q_\lambda(n) \cdot p_{n,g}(x)$$

The readout process of the charge adds extra noise - readout noise, that can be modeled by a Gaussian distribution with mean μ and variance σ^2:

$$N_{readout}(x) = \frac{1}{\sigma\sqrt{2\pi}} e^{\frac{1}{2}\left(\frac{(x-\mu)}{\sigma}\right)^2}$$

The total output distribution is modeled by convolving the output distribution from the gain register with the readout noise to give:

$$f(x) = h_{\lambda.g}(x) * N_{readout}(x)$$

Note that this result can be transformed to "counts" (digitized signal) distribution by dividing the electron numbers by a scaling factor [41]. The scaling factor also normalizes the values of the distribution, g, μ and σ, which are the camera properties except for λ, which varies from pixel to pixel.

The mean number of photon for each pixel i is modeled as:

$$\lambda_i^{bright} = t_{exp}(R_B \cdot \omega_i + R_D)$$
$$\lambda_i^{dark} = t_{exp} R_D$$

where t_{exp} is the exposure time, R_B is the detected fluorescence rate for an ion in the bright state (corresponds to $|S\rangle$ state), ω_i is the fraction of fluorescence collected by pixel m (the total fluorescence summed over the whole image is normalized: $\sum_{i=1} \omega_i = 1$) , and R_D is the fluorescence rate when the ion is in the dark state (corresponds to $|D\rangle$state) which contains scattered light and thermal dark counts (discussed in section 4.1 in [32]). λ_i^{bright} and λ_i^{dark} are taken into account for each pixel to build B_m and D_m - the dark and bright distributions, which has the shape of $f(x)$ and will be discussed in the next section. Another possible and interesting analysis of the camera's output distribution is the Poisson-Gamma distribution modeled by Hirsch et al. in [42].

3.3.2 State detection algorithm

The difference in intensities between the bright and dark states during the state selective fluorescence detection can be compared and utilized to set a discrimination threshold. The photon emission process follows a Poisson distribution with different detection-time dependent means. High detection fidelity is translated to a small overlap of the Poisson distributions for the "dark" and "bright" scenarios. The EMCCD output does not follow a Poisson distribution, as they are altered by camera readout noise, dark currents, and gain (see section 4.4.2). Thus, the differentiation of the camera dark and bright measurements is done by comparing the total intensity over a set of predetermined pixels of interest. A discrimination threshold is set to each ion individually using the following process: (a) Acquiring a batch of samples (around a few thousand) of "bright" and "dark" images. (b) The pixels are ordered from the brightest to the darkest according to the average of bright images. (c) The intensity distribution of each "dark" and "bright" images

compared for n brightest pixels, where n can get up to a single brightest pixel or a predetermined maximum number of pixels. (d) The optimal n (number of brightest pixels) is chosen by maximizing the mean distance of the distribution compared to the minimum distance (when there is no overlap) or by the minimal distribution overlap:

$$n_{optimal} = max\left(\frac{\bar{B}_n - \bar{D}_n}{\bar{B}_n - \bar{D}_n - \big(min(\bar{B}_n) - max(\bar{D}_n)\big)}\right)$$

Where $\bar{B}_n$,$\bar{D}_n$ represent the bright and dark intensity distribution for n pixels.

High separation of the two distributions (for the bright and dark state) implies that discrimination errors cannot be induced, and the distributions are separated by a large margin relative to the mean distribution. This discrimination is done for each ion separately, setting a threshold to each ion individually in a non-dependent way [25]. Exposure time is another factor that influences the quality of the discrimination. Shorter exposure times will decrease the distance between the distributions because fewer photons are collected, and the difference between the high photon count for the dark state and the low photon count for the bright state is getting closer. Although, for exposure time up to 700 μs the discrimination error is smaller than 1×10^{-4}. The number of pixels that are marked and used for the optimal n is around $9 - 12$ pixels per ion. This threshold and marked pixels will later be used in the live readout system and analysis to determine the state of the ions.

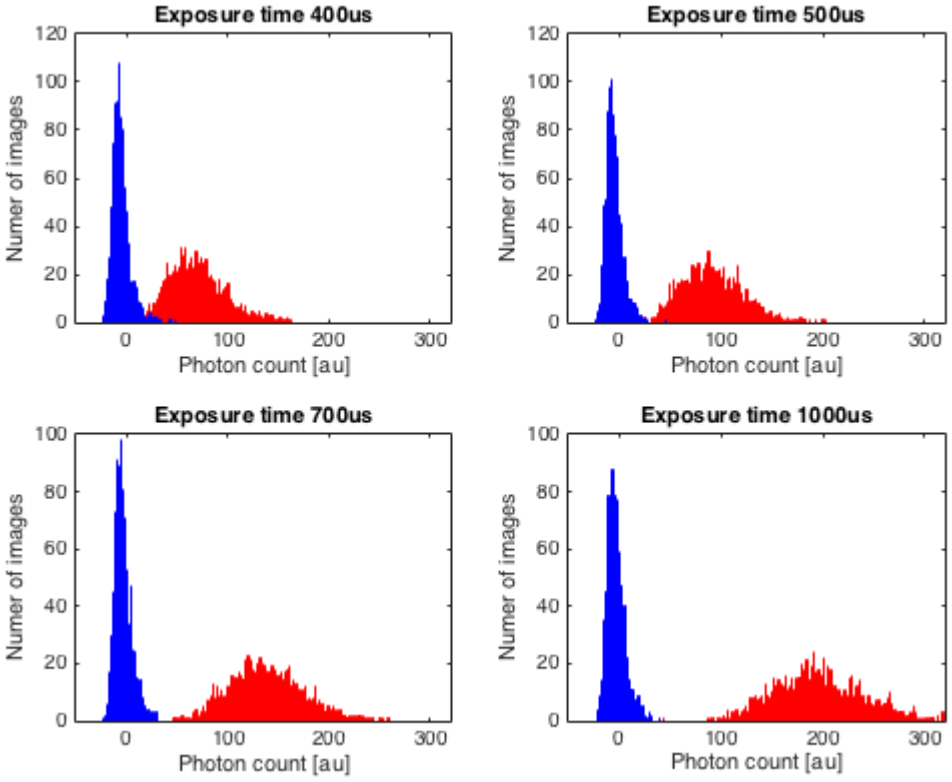

Figure 9: **Dark and Bright photon count distribution in [au].** An example of discrimination distribution of bright and dark states for various exposure times from $400\mu s$ to $1000\mu s$. We can see that the ability to discriminate correctly without overlapping the distributions for short exposure times is decreasing. The red distribution is the distribution of the bright states, and the blue is for the dark state. The dark state distribution centered around 0 photon count, where the bright state is broader and moves to higher photon count with longer exposure times. The optimal exposure time for this work is 700 μs, where we can significantly discriminate between both of the states.

Camera parameters:

The camera's magnification is determined by the ratio between the distance of each ion on the EMCCD, and the real inner distance of the ions in the trap. The inner distance between the ions is calculated in [43], using the formula $l^3 = \frac{Z^2e^2}{4\pi\epsilon_0 M\nu^2}$, giving a trap frequency of $\sim$ 600 KHz, and $l = 4.68$ the inter-ion distance is $l \cdot 1.077 = 5.04\ \mu m$. The pixel distance is measured using a Gaussian fit to an ion image to be 13.06 pixels, which translates to 209 μm. the total magnification will be:

$$Magnification = \frac{\text{Pixel distance}}{\text{Real distance}} = \frac{209}{5.04} = 41.46$$

This number agrees with the designed magnification ($\sim$ 40) that set by the numerical aperture, and its distance to the ions.

Fluorescence spectra:

In Sr^+ the excited state $5P_{\frac{1}{2}}$ can decay to the $5S_{\frac{1}{2}}$ but also to the $4D_{\frac{3}{2}}$ meta-stable state. This is the three-level Λ system. When the ion decays to the D manifold, the interaction with the laser that drives the $5S_{\frac{1}{2}} \leftrightarrow 5P_{\frac{1}{2}}$ transition stops until the ion will decay back to the ground state. Because the D manifold is a long-lived level ($\tilde{}390\ ms$), a repump laser that drives the $P_{\frac{1}{2}} \leftrightarrow D_{\frac{3}{2}}$ transition is needed - the 1092 nm laser. Due to the splitting of the Zeeman levels when the external magnetic field is applied, the level structure of the Sr^+ contains eight levels (a numerical solution of the optical-Bloch equations for the eight levels involved can be found in [30] a much more complicated system than the canonical 3-level Λ system. The Zeeman shift due to magnetic field B along the quantization axes is:

$$\delta\omega = g_j m_j \frac{\mu_B \left|B\right|}{\hbar}$$

with $g_j\left(S_{\frac{1}{2}}\right) = 2\ ;\ g_j\left(P_{\frac{1}{2}}\right) = \frac{2}{3}\ ;\ g_j\left(D_{\frac{3}{2}}\right) = \frac{4}{5}$ and m_j is the projection of the total angular momentum on the z-axis. We can scan the fluorescence spectrum of the ion using both the 422 nm laser and the 1092 nm laser in order to find dark resonances - a deep in the fluorescence spectrum. Dark resonance can teach us in a relatively simple way about the detuning of the drive laser. When both of the lasers are turned on, and the detuning is scanned, the dark resonance will occur when the detuning of the two lasers is equal with respect to a specific set of Zeeman sub-levels. The polarization of the lasers determines the number of dark resonance and their shape in the spectrum. The laser line-width sets the width of the dark resonances in the spectrum.

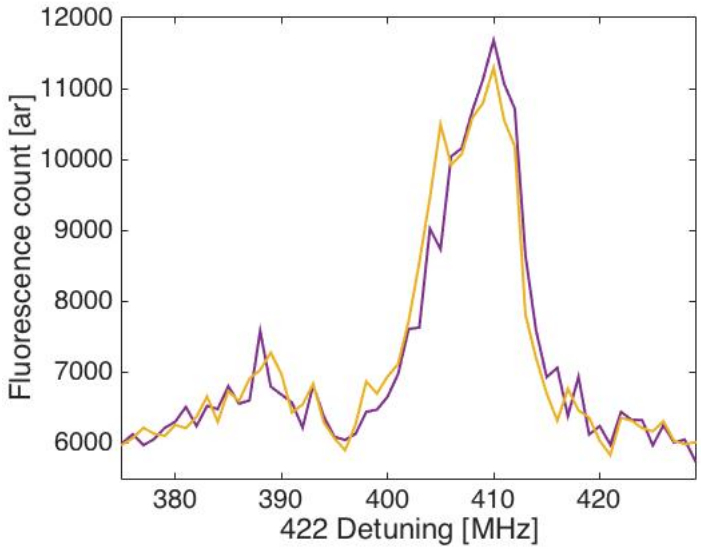

Figure 10: **Fluorescence spectra** measured in the lab. The $S_{\frac{1}{2}} \rightarrow P_{\frac{1}{2}}$ transition resonance with the 422 nm laser on two ions. The measurement shows the EMCCD's fluorescence count from the ion (in arbitrary units) as a function of the 422 nm detuning. The detuning is from the saturation absorption frequency (detuned 440 MHz from the $S_{\frac{1}{2}} \rightarrow P_{\frac{1}{2}}$ transition), And after it passes twice an AOM before it gets to the ions. The minimum of the fluorescence occurs at the 1092 nm repump detuning and it is due to dark resonance of the repump laser. The spectrum is asymmetric with respect to the red and blue detuning. When the laser is blue detuned it heats the ions where red detuned laser cools them.

4 Live readout, analysis and feedback

The detection of the ions state is done by detecting the fluorescence using a specially resolved detector: an EMCCD camera that transmits the digital images of the ions (before it is processed and analyzed) using two parallel paths: (a) the slow path, using the camera memory, and downloading the images to the PC using a USB 2 interface, and (b) the fast path, with live access to the data, right after the analog to digital converter (ADC) on the camera, using a Camera Link interface that follows by processing and analysis of the data on a FPGA frame grabber.

To coherently control the state of the ions, in order to perform tasks such as quantum error correction (that contains within the algorithm measurements and conditional operation), we need the ability to access the ion state before it will decohere - meaning, as closest to the measurement as possible and operate with the desired operation in that time scale. This chapter will describe the live readout and feedback system implemented in the lab.

4.1 Implementing live readout

The iXon Ultra used in the lab is equipped with a Camera Link output. Camera Link is a communication protocol that describes the transfer of a 2D data array, as pixels of an image. The camera streams the image data to an FPGA frame grabber, there we process and analyze it according to our needs. Camera Link provides access to the camera data output with very low latency, transferring 16-bit pixels at a rate of $40\,MHz$ per pixel. Before implementing this interface, the only access to the data was at the end of each experiment (that contains many repetitions thus many images), suggesting that to apply conditioned operations on the ions is only possible with the use of post-processing and post-selecting of images.

Connector	Camera Link (Base)	USB 2.0
Data transfer Rate	1.12 Gb/s	480 Mb/s
Max cable length	$10\,m$	$3m$
Estimated latency	~ ns	20 ms
Camera Control	Not implemented	Full control
Connector	26 pin	USB
Capture Board	Required FPGA	PC

Table 1: A comparison between the different Andor iXon Ultra 879 interfaces [44].

4.1.1 Camera Link interface

Before Camera Link, there was a lack of a communication standard in the vision industry between a camera and a frame grabber. There was an abundance of different connectors results in many cable types. The physical communication layer was not well defined as well as the data transfer protocol, camera timing, and camera singling. Camera Link is a solution to all of the above as it is a robust, complete interface between a camera and a frame grabber.

Protocol description

Camera Link is a serial communication protocol standard developed for vision applications (A full protocol description, can be found in [45]). The protocol is based on Channel Link technologies (by National Semiconductors) such as Low Voltage Differential Signaling (LVDS) as the communication channel. Each Channel Link transmmiter\reciver pair is made out of four LVDS pairs. LVDS is a physical communication channel that transmits the encoded information in the difference between two different voltages sent to the receiver and compared there. LVDS is a useful technology for vision due to its low noise and fast data rates

that allow a transmission of multiple streams of digital information [46]. The data transmitted is serialized $7:1$, with four data streams (7 bit on each stream) and a dedicated clock making it a total of five LVDS pairs.

The four LVDS data stream and clock, accepted by the receiver, which then drives the 28 bits and a clock to the board. There are four extra LVDS channels for camera control, but this was not implemented in our camera. Four of the 28 data signals (bits) are sync signals (also known as "enable signal"): Frame Valid (FVAL) for valid lines, Line Valid (LVAL) for valid pixels and Data Valid (DVAL) that supports cameras with low data rate (padding the transmission with dummy words) - always high in our camera. The fourth signal is spare. Hence, 24 data bits transmitted on a single cycle. The data stream only contains pixel data for the pixels within the camera user-defined region of interest (ROI), and hence the length of LVAL and FVAL will be dependent on the defined ROI. Camera Link interface has three configurations, Base, Medium, and full. Each of them allows for the transmission of different amounts of data, where the medium and full configurations require and extra cable.

The Andor Ixon Ultra 879 is supplied with a base configuration, transferring the data over three ports. Each of them is an 8-bit word, corresponds to 24 bits of pixel data, 3 bits of sync signals, and clock. Both the camera and the Frame grabber have a build-in MDR 26-pin connector optimized by $3M^{TM}$ that designed the cable as well. Base configuration bandwidth is up to 85 MHz giving a readout rate of $2.38\,Gbit/s$ [37, 47, 48, 49].

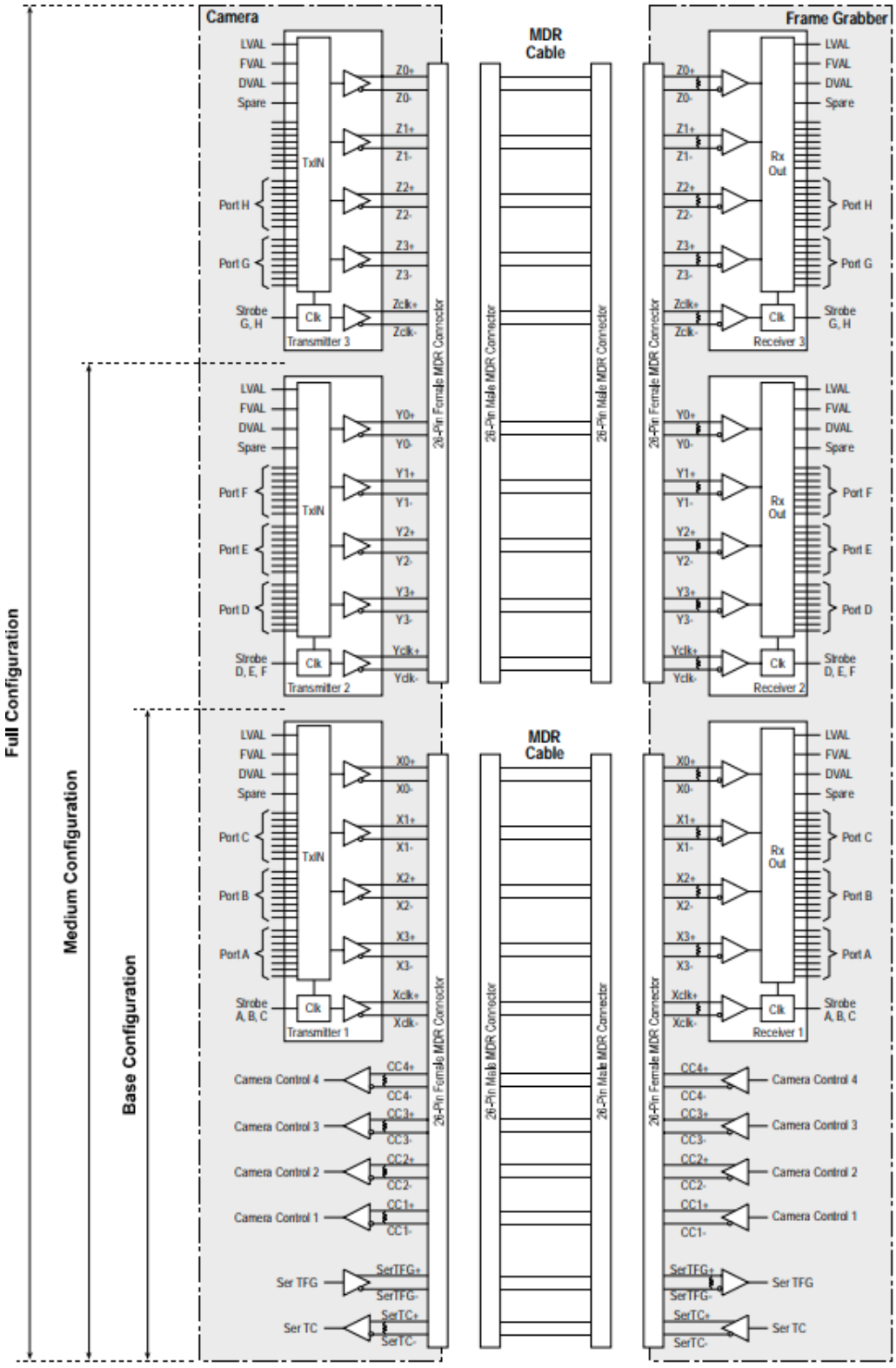

Figure 11: **Camera Link block diagram** contains Base, Medium, and Full configuration. The data is transmitted from the transmitter on the left (camera side) to the receiver on the right (Frame grabber). The ports are marked with capital letters. Ports A-C are in use for the base configuration. X, Y, and Z mark the LVDS channels. The base configuration uses channels $X_0 - X_3$. For each configuration, there is a dedicated clock LVDS channel. The Camera control and asynchronous LVDS (SerTFG, SerTC) are also present but not in use in the Andor Ixon Ultra. Image borrowed from [45].

Signals and acquisition

Through the Camera Link interface, the image is transferred pixel by pixel starting from the bottom right of the EMCCD. A rising edge of the Frame Valid starts the data acquisition while a falling edge of the same signal ends it. Line valid rising edge marks the acquisitions of a new line. A new line is sent when Line Valid is high, and a line end when line valid is low. When both the Frame Valid and Line Valid are high, a pixel is transmitted. The camera has an on-head FPGA that processes the information after the CCD. The camera streams the data to the Camera Link channel right after the pixels are read out serially by the ADC, but before the image is transferred to the USB buffer memory until they are downloaded to the computer.

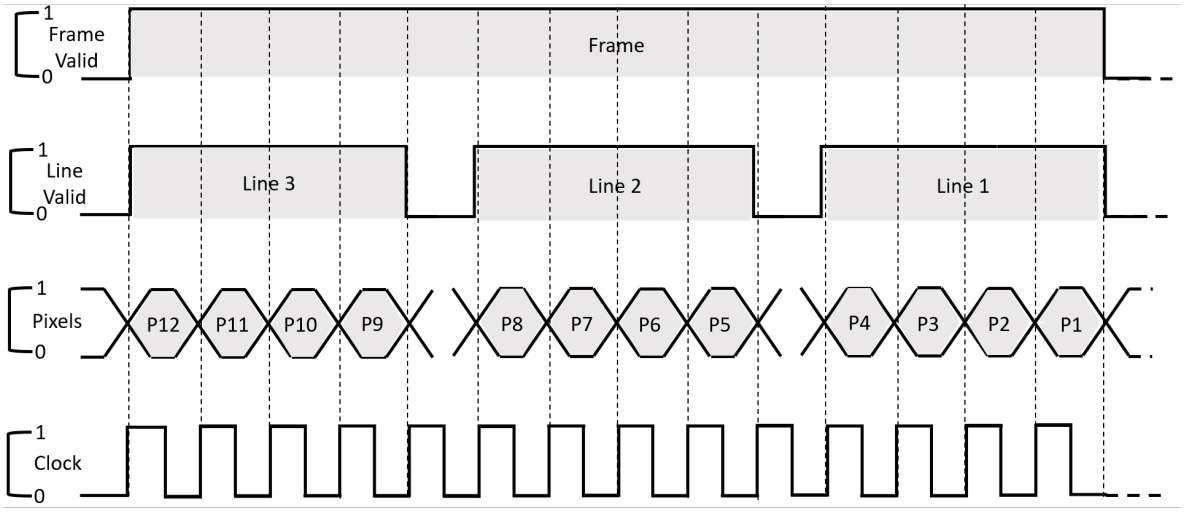

Figure 12: **Timing diagram of the Camera Link protocol.** Describes one image that contains three lines and four pixels on each line. Frame valid (FVAL) and Line valid (LVAL) are high at the start of a frame or a line, respectively. The pixels transmitted in series starting from the bottom right of the CCD. On each clock cycle that runs at a rate of $40MHz$, a pixel is transmitted only when both LVAL and FVAL are high. The diagram is not on scale because most of the readout time of the pixels is between a falling edge and a rising edge of a new LVAL. This time depends on the number of lines transmitted and the number of pixels in each line. The readout rate is combined form the vertical shift rate, horizontal shift rate, and the size of the storage that all together combine the readout time (see section 3.2.2).

Bit assignment

A Port is an 8-bit word. The ports are assigned to the Channel Link transmitter\receiver pair from the camera or to the FPGA frame grabber. In the base configuration, each of the 24 data bits are divided into three ports (also known as taps) that are

assigned to pins on the Channel Link interface. The configuration will determine the number of ports that the Camera Link uses in order to stream the data. The port is denoted by a capital letter starting from A that contains bits $0-7$. Ports A to C are used for the base configuration. The assignment of each bit in the ports is described in table 2. For images with a pixel depth of 16 bit, only ports A and B are used assigning bits $0-15$. The value of the transmitted pixel is divided by the two ports where port B contains the most significant bit, and A has the least significant bit (the building of the total pixel value is done on the frame grabber according to this logic). The bits of a pixel are not assigned to the Channel Link transmitters in a specific order but permutated as shown in 2. The camera pixel clock is at $40\,MHz$, giving $1.12 Gbit/s$ bandwidth.

Signal name	Pin name	16 bit pixel	LVDS Channel
Clock	TxClkIn/RxClkOut	Clock	Clock
LVAL	TX24/RX24	Enable	X2
FVAL	TX25/RX25	Enable	X2
DVAL	TX26/RX26	Enable	X2
Spare	TX23/RX23	Enable	X3
Port A0	TX0/RX0	Bit 0	X0
Port A1	TX1/RX1	Bit 1	X0
Port A2	TX2/RX2	Bit 2	X0
Port A3	TX3/RX3	Bit 3	X0
Port A4	TX4/RX4	Bit 4	X0
Port A5	TX6/RX6	Bit 5	X0
Port A6	TX27/RX27	Bit 6	X3
Port A7	TX5/RX5	Bit 7	X3
Port B0	TX7/RX7	Bit 8	X0
Port B1	TX8/RX8	Bit 9	X1
Port B2	TX9/RX9	Bit 10	X1
Port B3	TX12/RX12	Bit 11	X1
Port B4	TX13/RX13	Bit 12	X1
Port B5	TX14/RX14	Bit 13	X1
Port B6	TX10/RX10	Bit 14	X3
Port B7	TX11/RX11	Bit 15	X3
Port C0	TX15/RX15	nc	X3
Port C1	TX18/RX18	nc	X2
Port C2	TX19/RX19	nc	X2
Port C3	TX20/RX20	nc	X2
Port C4	TX21/RX21	nc	X2
Port C5	TX22/RX22	nc	X3
Port C6	TX16/RX16	nc	X1
Port C7	TX17/RX17	nc	X1

Table 2: **Bit assignment for a single 16-bit pixel.** The information about the pixel transferred to the Channel Link transmitter from three different ports, each connected to a different pin on the transmitter. A maximum of 28 bits can be transmitted over the four different LVDS channels. For a 16 bit pixel, the data is transferred from ports A and B, where port C is not connected. For an RGB image or a 24-bit image, port C is in use, and these pins are connected.

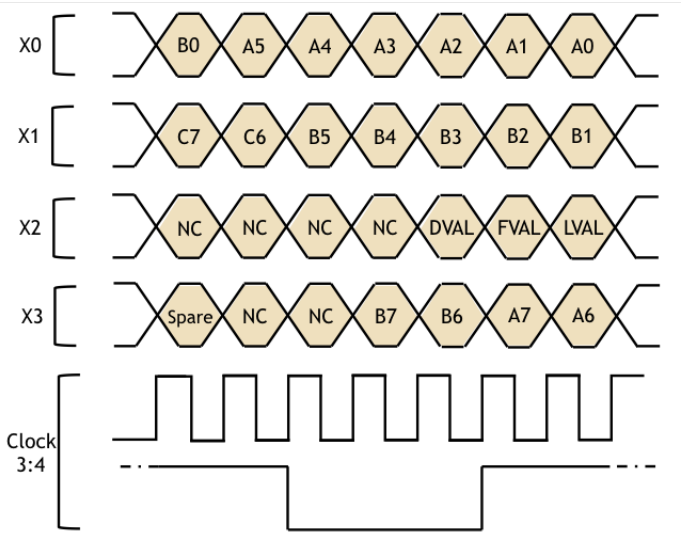

Figure 13: **Bit assignment for a single 16-bit pixel.** Illustration of the table above. Each channel contains 7 bits permutated from different ports. For example, one can see that channel X_0 contains pixels from port A and port B. The pixels timing diagram is a $7:1$, where the clock duty cycle is $4:3$, and the falling edge is after the second bit [47, 48].

4.1.2 Frame grabber

The ability to perform live readout is possible using a Camera Link communication protocol that connects to a dedicated FPGA device, with a Camera Link connector and image processing capabilities. For this task, we chose a NI-PCIe 1473R frame grabber card. This is a PCI Express (PCIe), user re-configurable Virtex-5 LX50 FPGA, aimed for image acquisition. This device has two Camera Link connection ports supporting Base, Medium, and Full configurations for Camera Link cameras [50]. The FPGA contains arrays of programmable logic blocks that allow for the user to implement programs (such as image processing) on the hardware level with rates independent of the load. The processing of information on the FPGA is done on-the-fly as the information arrives. Hence the ions state analysis time is limited by the readout time of the EMCCD and not by the image processing time of the FPGA. The FPGA frame-grabber is separated from the main FPGA that controls the experiment, implying that communication between the two FPGA's will be necessary to perform conditional feedback on the ions. The NI-PCIe 1473R frame grabber has two internal clocks. One of them is an image clock that is dedicated to reading the pixels coming from the camera, and its running at a $100\,MHz$ rate. This rate is 2.5 times faster than the pixel clock in the camera and promises that the pixels are read without loss or aliasing, following that $f_{sampling} > 2 \cdot Bandwidth$ is the Nyquist rate. The second clock is a $40\ MHz$ internal clock that runs all

the processing tasks of the frame grabber.

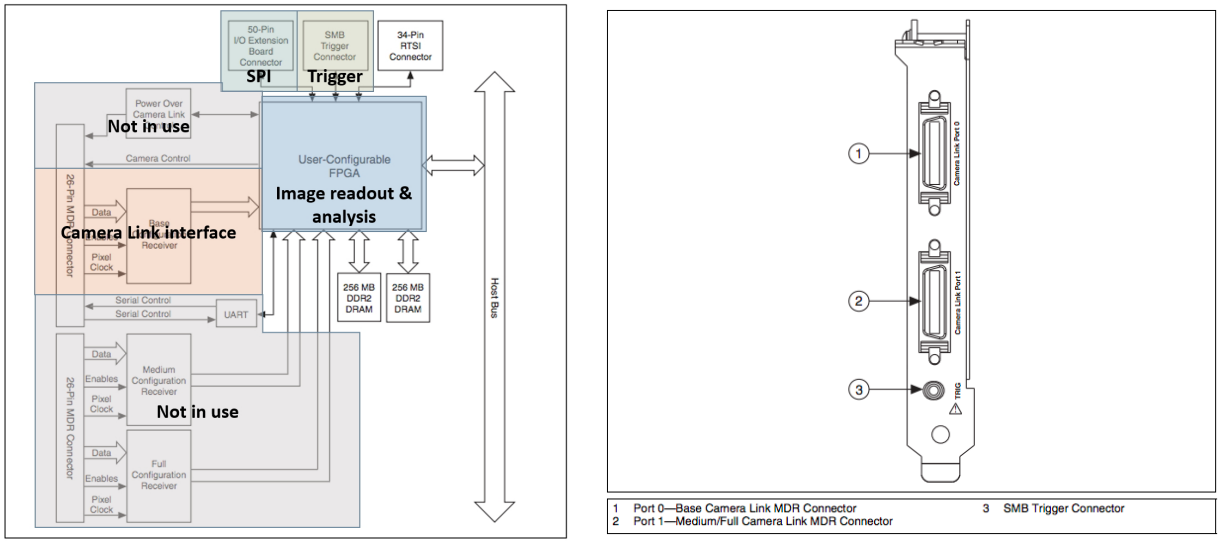

Figure 14: **NI 1473R PCIe hardware. Left:** the FPGA frame grabber block diagram. **Right:** NI-1473R-PCIe frame grabber connectors. The Camera Link cable connected to 1 - Port 0, which is a Base Camera Link MDR connector. 2 is the Medium/Full MDR connector, and 3 is an SMB Trigger connector that the camera trigger connected to from the FPGA and triggers both the frame grabber and the camera together (the sketch is borrowed from [50]).

4.2 Hardware architecture

As written in 4.1, the live readout implemented using a frame grabber FPGA card that is external to the FGPA that controls and manages our experiments. The integration of the frame grabber to the main FPGA was necessary and included a new set of communication lines that were added to the existing framework. This architecture is described in the following section.

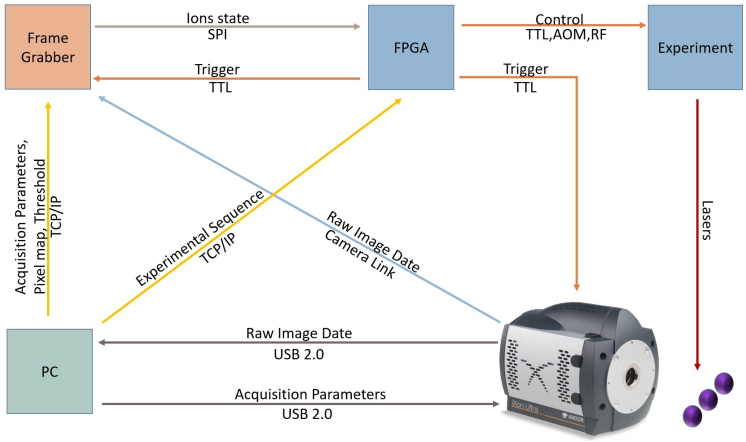

Figure 15: **Hardware architecture illustration** integrated in our lab. The different arrows represent the interfaces between all of the lab hardware, the data transmitted, and the kind of communication that connects between different devices. The FPGA is the heart of each experiment and controls all of the parts using TTL's, analog I\O's, TCP\IP, and SPI. Using Matlab on the PC, we are coding the time sequence of operations that will run in the experiment, setting the acquisition parameters for the camera, and sending the parameters of the experimental FPGA and frame grabber.

4.2.1 Communication architecture

This section describes the types of communication protocols used between the different interfaces that execute the live readout and feedback system:

TCP\IP is the communication protocol between the Matlab and the LabView host (that communicates with the FPGA card through the computers motherboard interface PCIe). Labview is the programing language with which we program the FPGA (instead of VHDL or Verilog). Matlab is the user interface that manages the experiment. The experiment is programmed, set, and analyzed in Matlab. To transfer data such as the experimental sequence or parameters, the communication between the Matlab on the PC, and the National Instruments FPGA card is through a TCP/IP protocol. TCP/IP is a communication protocol mainly used for the internet but is adequate for any network communication. It is built from layers and provides a robust, ordered, error-corrected stream of bytes between applications via an IP network[1].

Serial communication is the communication protocol that we applied between the frame-grabber and the main FPGA is Serial Peripheral Interface (SPI). SPI is generally implemented as a two-way communication that consists of four signals, but we chose to implement a simpler one: One-way communication with three signals: Chip Select (CS), Data, and Clock[2]. On the sending side (Frame grabber - the master side), when the CS is going low, the clock starts to toggle. On each falling edge of the clock, one bit of information is transferred. The transferred data is read out from a FIFO as an unsigned 8-bit number. This process practically serializes the data. During the transmission, the array is read bit by bit. When the slave (the main FPGA) receives a falling edge on the CS channel it starts to listen to the clock and the data channels - whenever there is a falling edge in the clock channel the data bit is saved into a binary array indexed according to

[1] https://en.wikipedia.org/wiki/Internet_protocol_suite

[2] https://www.ni.com/en-il/innovations/white-papers/06/developing-digital-communication-interfaces-with-labview

the clock counts. At the end of the transmission, we have an 8-bit binary word that is converted to an unsigned 8-bit number. The CS sending rate is at 4 Mhz, meaning it takes $\sim 4\mu s$ to send the data. The reading rate is 40 MHz to avoid under-sampling.

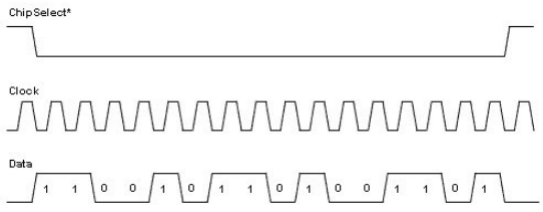

Figure 16: **SPI communication channels**. The Chip select sets the start of the data transfer. When CS falling edge detected, the clock line is being listened to, and with every rising edge, the information from the data channel is read. Each clock cycle is representing a different ion on the ion chain. For example, the data regarding the first ion will read on the first clock cycle, the second ion on the second clock cycle, until the entire array is readout. Every time the data signal is high, the information is acquired as Boolean 1, and in our case, translated into a "bright" state of the specific ion according to the clock cycle.

USB 2.0 is a standard specification for communication protocols, connections, and power supply between devices. USB 2.0 is the main communication layer between the camera and the computer: Sending through is the acquisition parameters to the camera before an experiment, setting the camera to start acquiring and reading out the images from the camera to the computer at the end of an experiment.

Camera Link The interface between the camera and the frame grabber FPGA is thoroughly described in section 4.1.1.

4.3 Software architecture

The programming of both the frame-grabber FPGA and the main FPGA is done using LabView - a visual programming language made as a development environment and a system-design platform from National Instruments. LabView allows us to maintain the communication with the FPGA on two levels. The higher one is the user interface (host) that runs on the PC and controls the operation of the main FPGA by reading or writing to the FPGA and communicating with Matlab (using TCP/IP). The lower level is hardcoded on the FPGA card itself, and usually, a machine type programming is needed (In our case, we have used LabView platform to program). The following section will describe and give

a detailed explanation of the software that we wrote for the live readout and feedback task.

4.3.1 Clock

FPGAs in general and frame grabbers, in particular, specialized in running computational tasks at a high rate. The LabView FPGA interface allows us to perform more efficient computations using a timed loop called Single-Cycle Timed Loop (SCTL). All functions inside this loop executed within one clock cycle (tick) of the FPGA selected clock. This means that not all the functions can be used inside a SCTL - a function that takes more than one tick, will not compile inside a SCTL. Not using a SCTL, will result in a slower execution rate where the default clock rate of the card is the maximum rate. The execution of functions outside of a SCTL loop can take longer, meaning some of the function will take one or more clock ticks to execute[3].

Frame grabber clocks:

Three main clock domains run in parallel on the frame grabber:

- Image readout and analysis - the main loop that is running on the frame grabber. Runs at a 100 MHz, 2.5 times faster than the camera pixel clock readout rate through the Camera Link interface. This loop reads out the pixel data and executes on-the-fly image analysis state detection.

- SPI - in this loop, the SPI communication protocol is implemented, running at a 4 MHz rate parallel to the previous loop where each tick of the loop sends 1 bit of information from the frame-grabber to the main FPGA.

- Memory readout - is a side loop that controls the reading of the pixel map from the memory of the frame-grabber after the primary discrimination process and before the experiment begins.

Main FPGA clock

- Main loop - runs the entire experiments in the lab. This loop controls the lasers, AOM's, trap frequencies, and the magnetic field. It also contains the condition loop that reads the ion state and acts by the results.

- SPI slave - the loop that is responsible for reading from the SPI channels and converts the data received from the frame-grabber into an integer number that corresponds to the ion state.

[3]https://knowledge.ni.com/KnowledgeArticleDetails?id=kA00Z000000P8sWSAS&l=en-IL

4.3.2 Live readout and image analysis

The image analysis is realized out on-the-fly during the readout. Before an experiment, the frame grabber is uploaded with information about the upcoming experiment - an updated pixel map, threshold parameters, and the number of repetitions uploaded to the frame grabber at the end of the discrimination process (see 3.3.2). The pixel map links between a pixel to an ion. For example, if after the discriminator process a pixel is relevant to ion number 3, in the pixel map, the cell that relates to this pixel location will get the number 3. If a pixel does not belong to an ion, it gets the number zero. The threshold is an array of integer numbers, each cell correspondent to an ion on the chain, and each ion is thresholded separably.

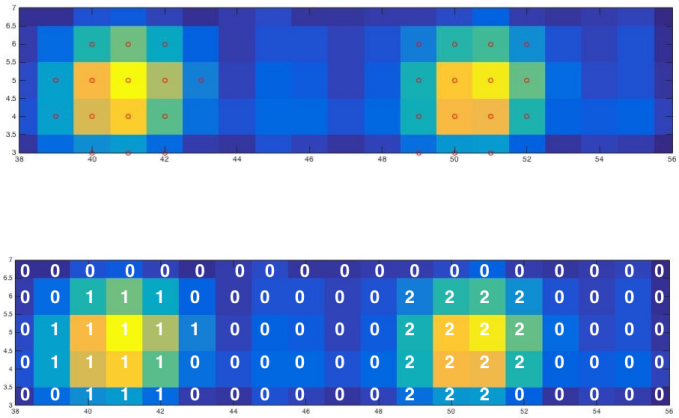

Figure 17: **Pixel map example**. On the top image, we can see the ions and the selected pixels that were selected to discriminate between dark and bright states according to the discrimination algorithm. The pixels are sorted from brightest to darkest, and only the most relevant pixels to each ion get selected. The total signal in these pixels is calculated and compared to a threshold in order to determine whether the ion's state is bright or dark. The bottom image shows the pixel map generated from the image above after the discrimination processes, overlayed on the image of the ions to demonstrates the meaning of each number. The ions are sorted left to right where the left most ion gets the number 1 and so on. This map is sent as a vector to the frame grabber memory. The memory is read during each pixel acquisition to relate each pixel to a specific ion.

When an experiment begins, the camera and the frame-grabber are triggered from the main FPGA with the same trigger. The camera starts to acquire the image, and the frame grabber waits for a Frame Valid rising edge. As mentioned in 4.1.1, the Camera Link sends four syncing signals. The frame grabber acquisition loop is working at a 100 MHz rate while the camera streams the pixels at a 40 MHz rate. When a Frame Valid arrives, the frame grabber knows that a new frame is now acquired. Once the Line Valid and Frame Valid are high, a new pixel

is acquired. Using the LVAL and FVAL signals to activate counters, each pixel has its coordinates, that are known during the pixel processing.

The pixels are read straight from the ports of the Camera Link interface. From the iXon Ultra 879, data is sent in 2 ports, A and B; each contains 8 bits of information, read separably, and joined to one 16-bit number where the B port has the most significant bit. After a one pixel reading cycle (takes about 5 ticks on the FPGA clock), the pixel coordinate and value are known, and the state analysis starts. The pixel coordinates are used to read a specific location from the frame grabber memory, where the pixel map is saved. As mentioned above, the information from this memory cell will link this pixel to a specific ion. The pixel's value is summed along with the rest of the pixels that relate to the same ion. This process is parallel to the readout. At the end of the image acquisition, the total sum of pixels for each ion is compared to a corresponding threshold value. The comparison result creates a binary array: 1 if the sum is larger than the threshold and 0 if not. These numbers translate to a "bright" state or a "dark" state, respectively. The binary array is translated to an unsigned 8-bit number and saved into a first in first out (FIFO) memory on the frame grabber. The FIFO is read on the SPI domain. At the end of an image acquisition, the data is serialized, and sent via SPI to the main FPGA at 4 MHz per bit. This process repeats until all the images in an experiment are acquired.

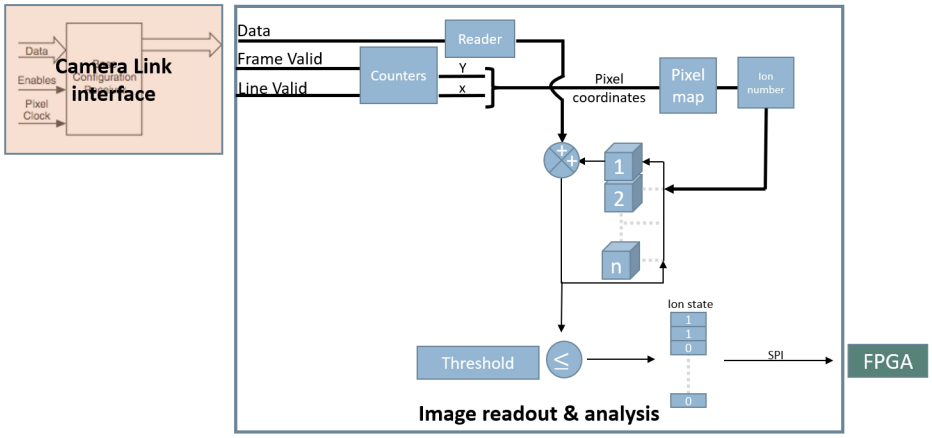

Figure 18: **Live readout and image analysis scheme.** The frame grabber listens to three different lines: Data line, which contains the information of the pixel value, Frame valid, and Line valid that translate to X and Y coordinates. These coordinates are used to read from the frame grabber memory the relevant ion number that links to this pixel, and then the pixel is summed with the rest of the related pixels. When FVAL is going low, it is the end of the image acquisition. Then the sum of the pixels is compared to a threshold value that results in a binary array. The array is sent to the main FPGA using the SPI interface. The entire image analysis time depends on the number of pixels. For one pixel, it will take 50 ns ($t = \frac{N_{tick}}{2.5 \cdot f_{CL}}$). This process is bounded by the readout time because the analysis is parallel to the readout from the camera. The readout time (~600 μs), along with the exposure time (700 μs) are almost as long as the qubit dephasing time (about ~ 2 μs) making these processes as the main holdback in performing quantum feedback.

4.3.3 Feedback architecture

In the main FPGA, the main loop that is running the experiment is programmed to work as a processor. Before each experiment, the experimental sequence is downloaded to the FPGA, row by row. The FPGA is executing the command in each row and, when done, moving forward to the next row. This type of execution is done using different cases, where each row in the code is translated to a case in the main loop. Using this architecture, the FPGA can jump between cases and even implement logical loops by jumping back in the row number. We are using this kind of architecture to implement the feedback option. When writing a sequence to run on the FPGA, one of the commands is an IF-Do case. Applying such a case, the FPGA waits for a variable contains the information about the ion state to arrive from the serial loop. This state compared to a pre-set value that is sent to the FPGA before the experiment. If the values are equal, a pre-defined operation, such as a gate or a rotation, is carried out. For different values, the

program enters an ELSE case (nested in the IF case) that loops over all the possible states.

4.4 Readout, noise source and implementation bugs

In order to implement the readout system in our lab, we started with a few sanity checks to find out if the system works as we expect it to work and delivers the same results as the offline discrimination process before integrating this into our lab.

4.4.1 readout fidelity

Readout fidelity will limit the correctness of our discrimination possibilities, thus limits the fidelity of any quantum algorithm we intend to execute using this system. The readout fidelity is calculated by comparing the results from the frame grabber discrimination processes to the results we get by post-processing the images using Matlab. We treat the post-processing results as the reference. (For more information about the camera's detection and processing done by Matlab see [25]). The fidelity is:

$$\frac{N-\epsilon}{N}$$

where N is the number of measurements, and ϵ is the number of errors. An error is counted when a difference between the live readout and the Matlab discrimination outputs excites. We evaluated the readout fidelity of the live readout system using a repeated initialization of the ions to a known sate (the initialization fidelity is from [51]), followed by a measurement. The discrimination is done by counting the pixels relevant to each ion. Different experimental parameters influence the readout fidelity: (a) Geometric ensemble of our set up (magnification, numerical aperture (collection efficiency), and spot size). (b) Noise - such as readout noise, noise factor, exposure time, and the image shape on the detector. (c) Physical properties of the experiment - radiation rate of $^{88}Sr^{+}$, ions state, ions distance (trap frequency), qubit coherence time, and the properties and stability of the laser (a problem in one of the lasers can affect everything such as the ion state, fluorescence rate, qubit coherence time initialization). (d) EMCCD hardcoded parameters such as Clock Induced Charge (see 3.2.2), noise, and quantum efficiency. All of these parameters influence in the same manner on both the live readout system, and the post-processing readout fidelity; thus, we expect to get identical results from both image processing paths. The readout fidelity of the system was tested in two ways. The first was to compare both pixel sums on each ion to make

sure it is identical, and the second was to compare the discrimination decision received both from the frame-grabber and the post-processing image. Both results found to be equal on over 2000 images, except for a bug case mentions in 4.4.3.

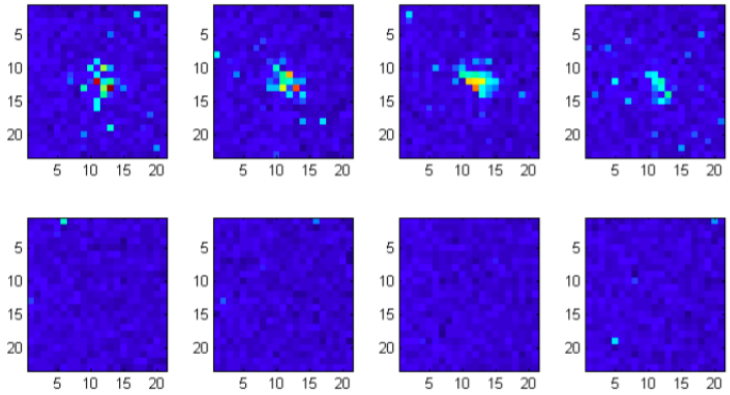

Figure 19: **Bright and dark images.** The top row shows bright images, whereas the bottom row is for dark images. In all of the images, the exposure time is 1 ms. There is a significant difference between the two images, as can be seen using the intensity distributions for $1ms$ in figure 9. The image is adapted from [25].

4.4.2 Noise

Noise can cause a wrong light distribution on the EMCCD, thus affect the discrimination fidelity - the overlap of the bright and dark distributions. Noise is present in all electronic systems. The presence of noise in an EMCCD and image processing is placing bounds on different parameters such as exposure time and readout time, which are the main holdbacks in this work. The exposure time is bounded from below for a couple of reasons. One of them is the photon collection efficiency, which is determined by the numerical aperture of the imaging system. The EMCCD's photon collection distribution is not Poissonian (like in Photon multiplier tubes); thus, the signal-to-noise ratio of an image is altered by the readout noise, dark current, and gain. This kind of noise is a limitation on two of the most time-consuming processes that can influence the fidelity and the ability to perform live readout and coherent feedback: exposure time and readout time. The numerical aperture is a giving property in our lab, and changing it is out of scope of this work. The features mentioned in this paragraph directly affect the ability to discriminate between the "dark" and "bright" state of the ion, and their presence may result in detection errors. Different noise sources that are relevant to our system are listed below.

Shot noise: is a statistical noise due to the particle nature of the photons. This noise obeys Poisson distribution with fluctuations equals to the square root of the signal: $N_{signal} = \langle I \rangle$. There is a signature to the shot noise both in dark and bright cases that affect the distribution of both states (see section 3.3.1).

Dark Current (thermal noise): is the thermal fluctuations within the EMCCD chip that are enough to eject electrons from the semiconductor body, which then contributes to the EMCCD signal. This called dark current and is known as reverse bias leakage current in non-optical devices and presents in all diodes. Dark current is caused by thermally generated electron-hole pairs, which build upon the pixels region even when are not exposed to light. It is one of the primary noise sources in image sensors. The sensor is cleared before an acquisition, but the dark current will still build up until cleared again. Thermal fluctuations of the voltage can be calculated using the Nyquist formula $\langle v^2 \rangle = 4Rk_BT\Delta f$, where R is the silicon resistance, k_B - Boltzmann constant, T - is the temperature and Δf- is the bandwidth of the EMCCD, from here we can understand that it can decrease by cooling the camera. The cooling of our EMCCD to $-80°$ reduces the thermal noise to such a low level that other mechanism dominates the dark count rate.

Clock-Induced Charge (CIC) noise: N_{CIC} is a noise source independent of the exposure time and exists for every pixel that is read out from the EMCCD camera. This noise mechanism is similar to the multiplication process, which is responsible for the gain of the EMCCD, and after the minimization of the thermal noise by cooling, this is the dominant noise source of the dark images. During the processes of moving charges from pixel to pixel, there is a probability that a hole will be accelerated by the clocked voltage and will collide with the silicon atom to produce a new electron-hole pair through impact ionization. In an EMCCD, the extra CIC electrons will be amplified by the gain register meaning there is no way to know if it is noise or photoelectrons. The probability of generating CIC noise depends on the number of transferred pixels. A small ROI, located as close as possible to the readout register, minimizes the amount of impact ionization possibilities, thus reduces the CIC noise.

Readout noise: this noise, σ_R is introduced during the pixel and line transfer towards the readout register at the bottom of the CCD. It happens due to the non-adiabatic excitation of electrons on the process. Readout noise can be considered as the CCD's detection limit, especially in the case of fast frame rate experiments because (a) dark current contributions will be negligible in short

exposures (b) faster pixel readout rates, such as 5 MHz and higher, result in significantly higher readout noise[4]. Luckily one of the fundamental advantages of EMCCD technology is that the gain -g is sufficient to reduce the readout noise to $\frac{N_{Read}}{g}$. Therefore high gains eliminates the detection limit, making the readout noise negligible.

Multiplicative noise: is the uncertainty inherent in the multiplying process that introduces additional noise. The fact that the gain process is stochastic adds to the fact that for one electron entering the gain register may result in a variety of possibilities for the number of electrons leaving it. This uncertainty is called "Noise Factor":

$$F = \frac{N_{out}}{g \cdot N_{in}}$$

Where $N^2_{in\backslash out}$ is the variance of the input and output signals to and from the gain register. In EMCCD technologies, the noise factor value is $\sqrt{2}$ [52]. This noise factor can be treated as an addition to the shot noise of the system (adding noise sources will increase the variation of readout electron number).

Quantum efficiency: the actual signal that the EMCCD generates is the number of electrons, or more accurately, "photoelectrons" that are created when a photon is absorbed. Photons of different wavelengths have different absorption probability, thus a different probability of generating photoelectrons. This probability is known as *quantum efficiency* or spectral response. The main contribution to quantum efficiency is the absorption coefficient of the silicon that serves as the bulk material of the device.

Total noise and signal to noise ratio

The total noise sources will eventually affect the signal to noise ratio. The different noise sources are summed in quadrature to give the total noise per pixel:

$$total\ noise = \sqrt{F^2 \cdot g^2 \left(N^2_{thermal} + N^2_{signal} + N^2_{CIC}\right) + N^2_{Read}}$$

The total noise is combined from the different noise sources that are amplified, thus multiplied by the multiplication noise $F = \sqrt{2}$ and by the gain g : the thermal noise, shot noise, and CIC noise. The signal that outputs from the camera can be simplified to $S = g \cdot QE \cdot p$, where p is the number of photons falling on a

[4]https://andor.oxinst.com/learning/view/article/sensitivity

pixel with quantum efficiency QE and gain g. The signal-to-noise (SNR) of the EMCCD camera (per pixel) is thus:

$$EMCCD\ SNR = \frac{S}{\sqrt{F^2 \cdot g^2 \left(N_{thermal}^2 + N_{signal}^2 + N_{CIC}^2\right) + N_{Read}^2}} = \\ = \frac{p \cdot QE}{\sqrt{F^2 \left(N_{thermal}^2 + N_{signal}^2 + N_{CIC}^2\right) + \left(\frac{N_{Read}}{g}\right)^2}}$$

We assume that P photons falling on the camera's pixel with a quantum efficiency QE generates S electron, which will be our signal. The incoming photons have an inherent noise variation to the signal itself (that the shot noise), which is the square root of the signal falling on the camera $N_{signal} = \sqrt{p \cdot QE}$. In our camera, due to the fact it is cooled down and operated in a low noise regime, the thermal and CIC noise can be neglected. Thus, simplifying the SNR to:

$$SNR = \frac{p \cdot QE}{\sqrt{F^2 N_{signal}^2 + \left(\frac{N_{Read}}{g}\right)^2}}$$

From here, we can see that increasing the gain, the readout noise becomes negligible, making our system shot noise limited [37]. Note that P takes into account the photon's probabilistic feature, thus can also be expressed as $p = R_B \cdot t_{exp}$, where R_B is the detected fluorescence rate and t_{exp} is the exposure time.

4.4.3 Bugs

This is a technical section that is relevant only to specific modes of operations when using the live readout system. During the readout system operation, we have noticed that for some parameters, the system is not working correctly or not at all.

Line Scan mode The camera's ROI is defined in a portrait mode ($x > y$) or Line scan mode ($y > x$) where x,y are the number of columns and rows respectively. The geometry of our problem - a chain of trapped ions, requires us to work in a portrait mode where the number of rows is varying between 4-6 rows, and the number of columns is limited by the EMCCD size (or more accurately the number of ions). When working with a single ion, the image ROI is usually a square ($x = y$), but sometimes y (by mistake) can be larger than x. If this happens, the camera sends the first row data via Camera Link (LVAL) before the rising edge of

the FVAL. When the frame grabber receives LVAL without FVAL, it treats this excess LVAL as a new image with one line and processing the rest of the image correctly without the first line. This results in two problems - the number of counted images is doubled (one for the single line and another one for the whole image for every image), and the sum of the counted pixels is wrong due to the fact a line is missing. The solution for this bug is to make sure that the number of rows (y) will always be smaller than x (relevant only for one ion).

Missing pixels in the first row We have noticed that regardless of the image geometry, when the first line is read through the Camera Link interface, there are missing pixels, whereas the rest of the lines are correctly read. The number of missing pixels is always:

$$\#\text{ of columns - }\#\text{ of rows}$$

This means that when the first line arrives, the LVAL first signal is shorter than the actual length of the lines. This is a problem that affects the counting of the pixels during acquisition. As mentioned in section 4.3.2, each pixel is counted. The counter acts as coordinates to compare to the pixel map and relate each pixel to its ion. Missing pixels will get out of sync with the pixel counting. Because each ion has a small number of pixels related to it and is needed for the threshold comparison, missing pixels can lead to a wrong sum and, by that, a wrong discrimination. The solution we have found for this problem is to change the camera ROI such that the missing pixels will not have any valid information and to reduce those pixels from the pixel map sent to the frame grabber.

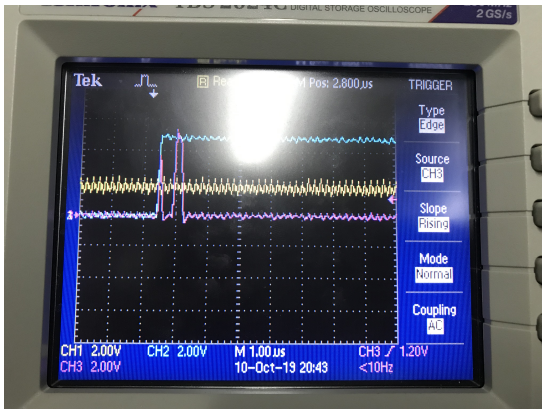

Figure 20: **Shorter line valid**. This photo is from a scope where the blue line is the frame valid, purple - line valid and, yellow - data valid. This is an example of a first LVAL shorter in time than the second line.

5 Results

This chapter contains the results of the experiments conducted using the live readout and feedback system integrated into our lab. We conducted three different experiments, starting with the simplest one containing one ion and incoherent feedback, all the way up to a two-ions experiment that show coherent feedback using entanglement. Using the live readout and feedback system changes the sequence of our experiments. Instead of a single measurement at the end of each repetition, another measurement is added after some combination of gates. According to the first measurement, the feedback process will initiate, and a second measurement follows. Note that the images now have two paths of processing - one is online, through the Camera Link and frame grabber, and the second path is going from the camera memory, though a USB 2.0 port to the PC and processed at the end of last repetition. This is true for all of the images, regardless of the feedback process. It is worth mentioning that since the images are read from the bottom right of the EMCCS, we have located the ions on that area of the EMCCD using a Dove prism to align the chain horizontally and then mirrors move it to the corner to shorten readout times. The ROI was also strictly chosen according to the limitations presented in the previous section.

5.1 One qubit feedback

This experiment was simple and used as a benchmark for the system parameters. We were interested in testing the ability to manipulate a qubit state according to its previously measured result. This was the first use of the live readout and feedback system in our lab. The qubit is initialized to the ground state at the beginning of each repetition. Then, applying a $\frac{\pi}{2}$ pulse using the 674 nm laser, the ion evolves to a superposition of the ground and excited state: $\frac{1}{\sqrt{2}}\left(\left|S_{\frac{1}{2}}\right\rangle + \left|D_{\frac{5}{2}}\right\rangle\right)$. While the qubit was in a superposition, we measured its state. The measurement collapses the ion superposition to $|S\rangle$ or $|D\rangle$ with equal probability. From this kind of measurement, we expect to get an equal distribution of "Bright" Vs. "Dark" states when we analyze the images at the end of the experiment.

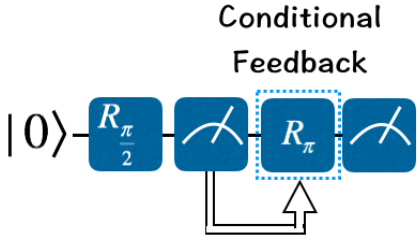

Figure 21: **Quantum circuit diagram representing the experimental sequence**. Using these diagrams is very common and useful. In the quantum circuit representation, each line is an ion. An operator is visualized as a square on the ion\s and a measurement as a meter. In this experiment, the ion is initialized to the ground state - $|0\rangle$ and was measured twice: the first measurement is performed after a $\frac{\pi}{2}$ rotation around the $\hat{x}$ axis, when the qubit is in a superposition. The second measurement is taken after the feedback - a π pulse that is only applied if the qubit was detected in the dark state ($|D\rangle$) in the first measurement.

After the qubit is measured, and the image was analyzed using the live readout system, feedback can be implemented. If the first measurement outcome is "dark", a π pulse is applied that takes the population form "dark" to "bright" (This is an arbitrary choice of states, the opposite experiment is possible as well). The expected results of the 2nd measurement (if the live feedback system is working) will be a distribution of only "bright" states.

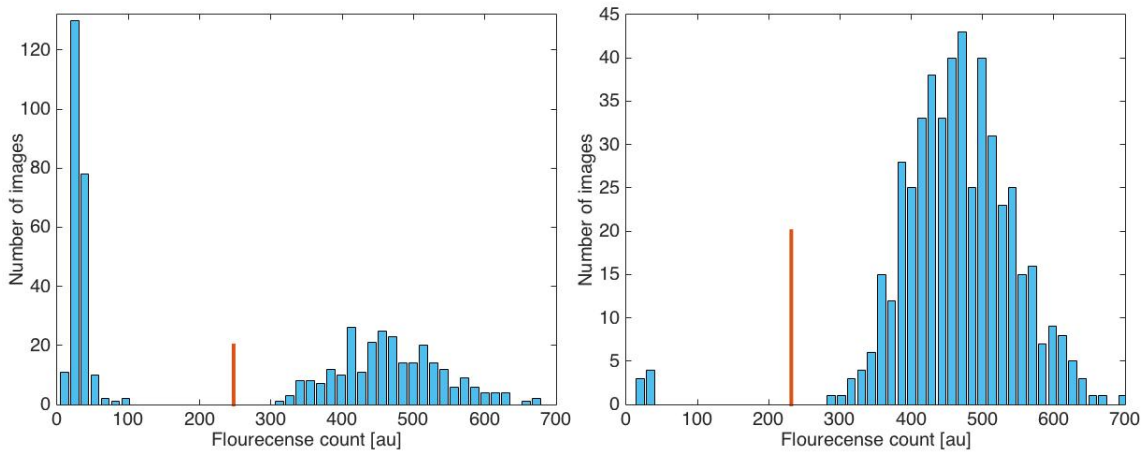

Figure 22: **One-qubit experiment results.** Each experiment contained two measurements, and in total 500 repetitions (1000 images). At each sequence, the first measurement gives the input for the feedback. Whereas the second measurement is taken in order to analyze the results and test the feedback performance. Figure 21 describes the experimental sequence. **Left**: The first measurement fluorescence count distribution in arbitrary units. The measurements are distributed between the dark state (low fluorescence) and the bright state (high fluorescence) almost equally as expected, given the fact that a $\frac{\pi}{2}$ pulse was operated before the measurement putting the ion in a superposition: $\frac{|S\rangle+|D\rangle}{\sqrt{2}}$.

The solid red line represents the threshold set in the calibration stage before the experiment. **Right**: fluorescence count of the second measurement in each repetition. As expected after a conditioned π pulse, the qubits' final state is always bright, although the initial state of the qubit after the measurement can be bright or dark. According to this result, the fidelity of the entire process is $0.986 \pm 0.04\%$ (this includes π pulse errors, and detection errors form both the frame grabber and Matlab).

5.2 Two-qubit feedback

Moving from one to two qubits increases the complexity of the experiment and allows us to test more exotic properties of the system, such as coherence, entanglement, and parity. The experiments relied mostly on Ramsey spectroscopy: in a Ramsey experiment, the state is initialized to $|\psi_i\rangle = \left|S_{\frac{1}{2}}\right\rangle$, followed by a $\frac{\pi}{2}$ pulse that rotates our qubit into

$$|\psi_{t=0}\rangle = \frac{1}{\sqrt{2}}\left(\left|S_{\frac{1}{2}}\right\rangle + e^{-i\phi_0}\left|D_{\frac{5}{2}}\right\rangle\right)$$

Where ϕ_0 can be set to zero. The qubit performs precession in the rotating frame during time evolution at a frequency equals to the detuning, making the phase difference between the superposition states evolves at $\delta(t)$, thus the state of the qubit would be

$$|\psi_t\rangle = \frac{1}{\sqrt{2}}\left(\left|S_{\frac{1}{2}}\right\rangle + e^{-i\int_0^\tau \delta(t)dt}\left|D_{\frac{5}{2}}\right\rangle\right)$$

Finally, a second $\frac{\pi}{2}$ pulse is applied while scanning the pulse phase and measuring the qubit state. By scanning the phase of the pulse, we measure the direction of the Bloch vector in the equator plane of the Bloch sphere which results in

$$|\psi_f\rangle = cos\left(\frac{\phi_f + -i\int_0^\tau \delta(t)dt}{2}\right)|S\rangle + sin\left(\frac{\phi_f + -i\int_0^\tau \delta(t)dt}{2}\right)e^{i\phi_f}|D\rangle$$

From here, the probability of measuring a "dark" state will be:

$$P\left(|D\rangle\right) = |\langle D|\psi_f\rangle|^2 = sin^2\left(\frac{\phi_f + -i\int_0^\tau \delta(t)dt}{2}\right)$$

Scanning the phase will outcome a Ramsey fringe. Note that $\delta\left(t\right)$ can be random as a result of frequency noise.

Another technique that we have used during the two-qubits experiments is *selective readout* of the qubits - placing one of the qubits "in hiding". This means that one of the qubits' superposition is coded in levels that are not affected during the detection, and by that, the information of that qubit remains protected. In our case, this superposition is coded on the $4D_{\frac{5}{2}}$ manifold using the $\pm\frac{3}{2}$ Zeeman splitting of the level $\frac{1}{\sqrt{2}}\left(\left|D_{\frac{5}{2},-\frac{3}{2}}\right\rangle+\left|D_{\frac{5}{2},\frac{3}{2}}\right\rangle\right)$. The qubit that is put in hiding is the one we are interested in "protecting" - keeping its quantum state. The unprotected qubit remains in the $\frac{1}{\sqrt{2}}\left(\left|S_{\frac{1}{2},\frac{1}{2}}\right\rangle+\left|D_{\frac{5}{2},\frac{3}{2}}\right\rangle\right)$ superposition. The sequence of selective readout starts after the qubits are in a superposition. Then, a global RF π pulse changes the population in the $\left|S_{\frac{1}{2},\frac{1}{2}}\right\rangle$ state to $\left|S_{\frac{1}{2},-\frac{1}{2}}\right\rangle$. This pulse is followed by an individual addressing (IA) π pulse of the 674 nm laser (consists of a global $\frac{\pi}{2}$ pulse with frequency corresponds to the $\left|S_{\frac{1}{2},-\frac{1}{2}}\right\rangle\rightarrow\left|D_{\frac{5}{2}',-\frac{3}{2}}\right\rangle$ transition, an AC stark shift pulse which is far detuned, and another global $\frac{\pi}{2}$ pulse [25]) only on the qubit we are protecting. At the end of the sequence, a global RF π pulse with the opposite phase puts back the unhidden ion in $\left|S_{\frac{1}{2},\frac{1}{2}}\right\rangle$ state. After this pulse sequence, the qubits are in $\frac{1}{\sqrt{2}}\left(\left|S_{\frac{1}{2},\frac{1}{2}}\right\rangle+\left|D_{\frac{5}{2},\frac{3}{2}}\right\rangle\right)\otimes\frac{1}{\sqrt{2}}\left(\left|D_{\frac{5}{2},-\frac{3}{2}}\right\rangle+\left|D_{\frac{5}{2},\frac{3}{2}}\right\rangle\right)$ state. In this state, the protected qubit will not be affected during the detection time because the $|D\rangle$ manifold does not couple to the 422 nm laser. During the measurement time, the hidden qubit can suffer from dephasing due to fluctuating magnetic fields. To mitigate this effect, we added an RF π pulses at specific times on the hidden qubit during the measurement time (which contains the exposure time and the readout time) . This is a generalization of the well known Hahn echo (for more details see [53]).

5.2.1 Coherent feedback

This experiment shows the ability to coherently control the qubits in a general superposition. We have applied the experiment as a conditioned Ramsey scan with adjustments: measuring one of the qubits followed by a conditioned operation done on the second qubit according to the outcome of the first measurement.

The qubits are initialized to a superposition with a global $\frac{\pi}{2}$ pulse rotating them to the state:

$$|S\rangle_1\otimes|S\rangle_2\rightarrow\frac{1}{2}\left(|SS\rangle+|DD\rangle+|DS\rangle+|DD\rangle\right)$$

In order to enable the feedback process afterward, we want to measure only one of the qubits and, by that, keep information regarding the superposition. This is done by "hiding" the second qubit in the D manifold, which is not affected by the measurement.

After one of the qubits is in hiding, we measure the state of the other qubit, while during this time, four echo pulses on the hidden qubit are performed (two during the exposure time (700 μs) and two during the readout time (600 μs)). The measurement will collapse the first qubit to one of the states - $|S\rangle$ or $|D\rangle$, while the second qubit remains hidden and in a superposition. After the measurement, we use the same technique to unhide the 2nd qubit in a reverse order of operations, mapping it back to the $\frac{1}{\sqrt{2}}(|S\rangle + |D\rangle)$ superposition. The unhiding is followed by a conditioned $\frac{\pi}{2}$ pulse on the second qubit (the one that we did not measure): if the measurement result is a "bright" state (the first qubit is in the $|S\rangle$ level), an IA $\frac{\pi}{2}$ pulse with scanned phase φ will follow. Whereas if a "dark" state was measured, the same IA $\frac{\pi}{2}$ pulse is applied but with a $\varphi + \pi$ phase. A measurement of the qubits will follow both options. If the qubits remain coherent during the measurement, meaning we will still have a defined phase between the $|S\rangle + e^{i\varphi}|D\rangle$ state and the laser, we can expect to see a Ramsey fringe. By projecting the state on one of the outcomes of the first measurement, we can calculate the expected outcome of this measurement for a bright state

$$\begin{aligned}
\langle S_1|\psi\rangle &= \left|\langle S_1|\left(i\frac{\pi}{4}\left(\mathbb{1}\otimes\left(cos\left(\phi\right)\sigma_x + i\sin\left(\phi\right)\sigma_y\right)\right)|S_1S_2\rangle + |S_1D_2\rangle\right)\right|^2 \\
&= \left|\frac{1}{2} + \frac{1}{2}i\left(\cos\left(\phi\right) + i\sin\left(\phi\right)\right)\right|^2 \\
\text{Dark population} &= 1 - \left|\frac{1}{2} + \frac{1}{2}i\left(\cos\left(\phi\right) + i\sin\left(\phi\right)\right)\right|^2 \\
&= \frac{1}{2}\left(1 - \sin\left(\phi\right)\right)
\end{aligned}$$

(When we analyze our result we look at the dark counts thus the calculation is done for the dark population explaining the use of $1 - |\langle\psi|\psi\rangle|^2$). The calculation for measuring $|D\rangle$ on the first ion:

$$\begin{aligned}
\langle D_1|\psi\rangle &= \left|\langle D_1|\left(i\frac{\pi}{4}\left(\mathbb{1}\otimes\left(cos\left(\phi+\pi\right)\sigma_x + i\sin\left(\phi+\pi\right)\sigma_y\right)\right)|D_1S_2\rangle + |D_1D_2\rangle\right)\right|^2 \\
&= \left|\frac{1}{2} - \frac{1}{2}i\left(\cos\left(\phi\right) + i\sin\left(\phi\right)\right)\right|^2 \\
&= \frac{1}{2}\left(1 + \sin\left(\phi\right)\right)
\end{aligned}$$

From these results, we can expect that if the conditioned operation works properly, the measurements will yield two Ramsey fringes with the opposite phase, with an

even $\frac{1}{\sqrt{2}}(|SS\rangle + |DD\rangle)$ or odd $\frac{1}{\sqrt{2}}(|SD\rangle + |DS\rangle)$ parity.

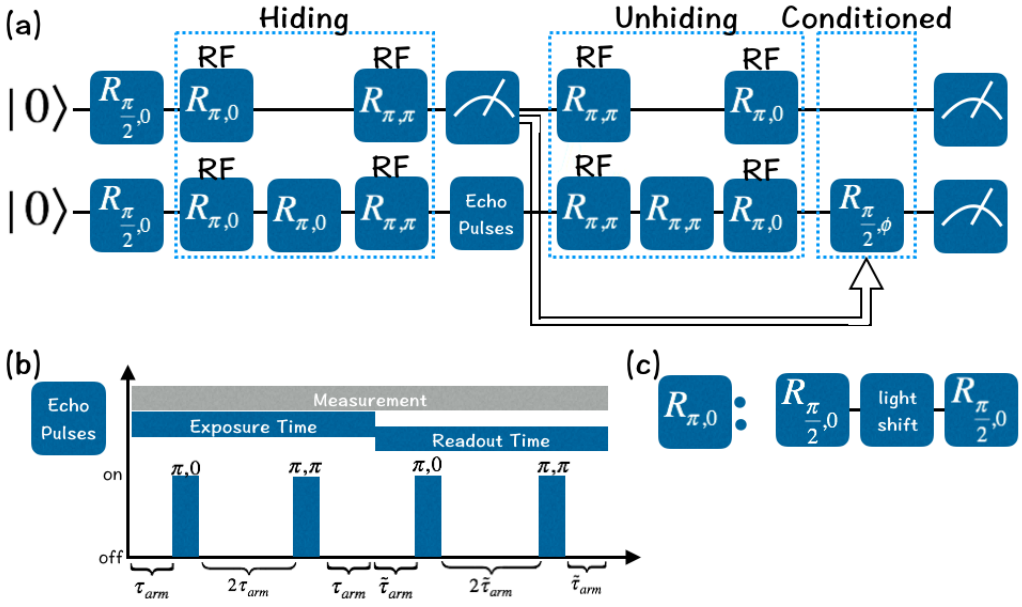

Figure 23: **Circuit representation of the experimental sequence**. **(a)** full experimental sequence after the initialization of the qubits. For example, $R_{\frac{\pi}{2},\pi}$ represents a 674 nm $\frac{\pi}{2}$ pulse with phase π. The double-lined arrow represents classical information. **(b)** image shows the RF pulse sequence when applying echo pulses on the second qubit during the first qubit's measurement. τ and $\tilde{\tau}$ represent the time between each pulse and is calculated as $\frac{t}{2 \cdot N}$ where t is the exposure time or readout time, and N is the number of desired echo pulses. **(c)** Detailed individual addressing (IA) pulse. IA π pulse contains two global $\frac{\pi}{2}$ pulses with the same phase and in between an AC stark shift pulse to reduce crosstalk between the qubits (for more details see [25]).

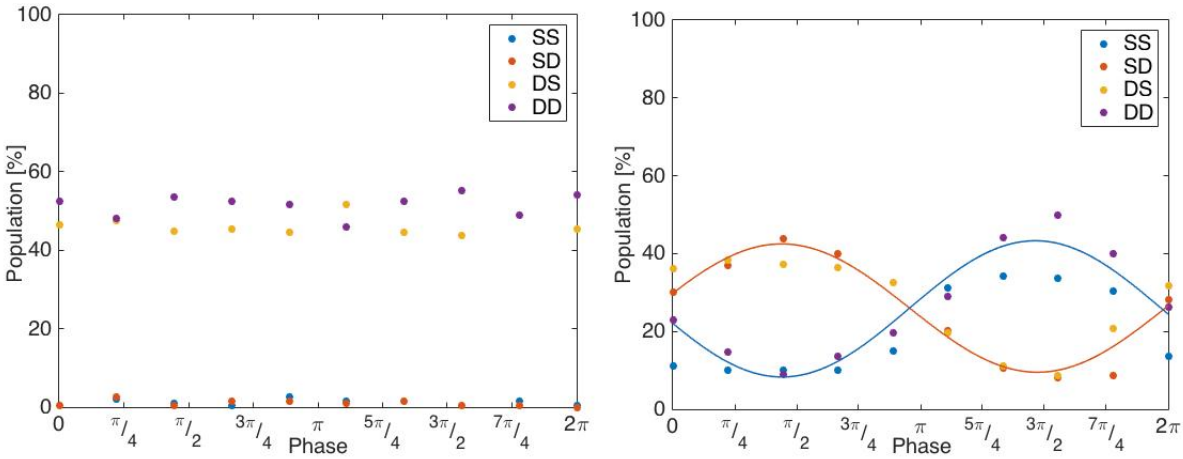

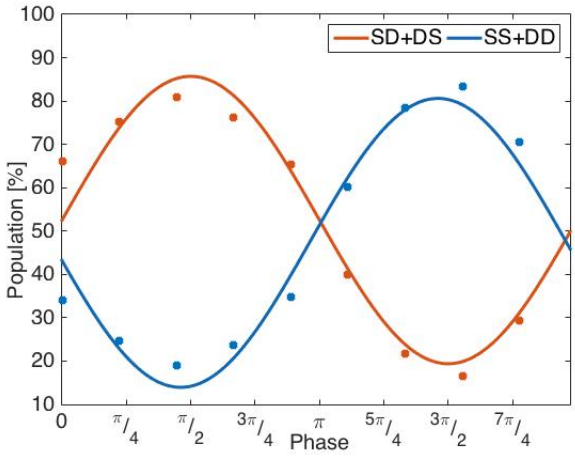

Figure 24: **Coherent feedback experiment results. Left:** First measurement result. The second qubit is not measured because it is hidden (the population of the second qubit to be in the bright state is around zero). The D manifold's magnetic susceptibility is 1.68 $\frac{MHz}{G}$ compared to the $S_{\frac{1}{2},\frac{1}{2}} \leftrightarrow D_{\frac{5}{2},\frac{3}{2}}$ which has a susceptibility of 1.12 $\frac{MHz}{G}$. However, The susceptibility of the $D_{\frac{5}{2}.\frac{3}{2}} \leftrightarrow D_{\frac{5}{2}.-\frac{3}{2}}$ transition we are hiding on is $3 \cdot 1.68 = 5.04$ $\frac{MHz}{G}$ which is 4.5 times larger than the $S_{\frac{1}{2},\frac{1}{2}} \leftrightarrow D_{\frac{5}{2},\frac{3}{2}}$ transitions. Thus we are prone to decoherence due to magnetic noise. This will affect the coherence of the conditioned operation and can also result in the unhiding fidelity, which implies that not all the population will be unhidden. **Right, bottom:** population of the four possible states after the second measurement, followed by conditional feedback on the second qubit. We can see the two Ramsey fringes: one for the even parity and one for the odd parity. After the first measurement, a conditioned individually addressed $\frac{\pi}{2}$ pulse with a specific phase is applied only on the second ion. For a bright state, a pulse with phase φ was applied and for a dark state measurement: $\varphi + \pi$. Each data point is 300 repetitions. **(c)** the sum of the different parity states and a fit to a sin function. The fidelity is calculated by the peak to peak ratio divided by two added to the chance probability (50 %) and is about $\sim 82\%$

5.2.2 Coherent feedback on entangled qubits

One of the main motivations to build the live feedback system is the ability to perform quantum error correction. As mentioned in section 2.2, some QEC protocols require conditional coherent manipulation on entangled states after a measurement of some of the qubits. The following experiment was designed not to test the system capabilities but to demonstrate quantum mechanical properties of the qubits with the live readout and feedback system. In practice, we generated an entangled state from two ion-qubits using an MS gate. We measured one of the qubits on a different basis (x base- after a Hadamard gate) collapsing the 2nd

qubit on the x basis, thus protecting its superposition. The results are interpreted as Ramsey interference.

The qubits are initially Doppler cooled, and optically pumped to a chosen Zeeman sub-level of the $5S_{\frac{1}{2}}$ manifold. They are then cooled to the radial and axial ground state using EIT cooling, and resolved sideband cooling that generates a $\bar{n} < 1$ state. After initialization, the entangled state $\frac{|SS\rangle+e^{i\varphi}|DD\rangle}{\sqrt{2}}$ is prepared from the two qubits using an MS gate (gate fidelity of 97%). Next, we operated with a Hadamard gate only on one of the qubits (for example, qubit #1) using individual addressing that allows us to operate on each of the qubits separately and not just with a global beam [25]. The Hadamard gate is implemented as a $\pi/2$ pulse around the x-axis. After this operation, the state of the qubits will be:

$$(|S\rangle + |D\rangle)_1 |S\rangle_2 + (|S\rangle - |D\rangle)_1 |D\rangle_2 .$$

Following the Hadamard gate, we protected the second qubit state by performing a hiding sequence (as described in 5.2) followed by a measurement of the first qubit. During the measurement, we applied four echo pulses on the hidden qubit: two RF π pulses with opposite phase during the exposure time ($700\,\mu s$), and another two during the readout time ($600\,\mu s$). The echo pulse sequence is described in figure 23 (c). The magnetic susceptibility of the D manifold where the qubit is in hiding is large, and without the echo pulses, the state completely decohere. Figure 26 left, shows the results from the first measurement. Since the qubits are entangled, and the first qubit was measured in the $\hat{x}$ basis (after applying the Hadamard gate) the second qubit will collapse to one of the following superpositions also in the $\hat{x}$ basis:

$$(I)\ \ |S\rangle_1 \left(|S\rangle + e^{i\varphi}|D\rangle\right)_2$$
$$(II)\ \ |D\rangle_1 \left(|S\rangle - e^{i\varphi}|D\rangle\right)_2$$

The phase is scanned as part of a conventional Ramsey experiment, meaning that given the measurement result of qubit #1, a global $\frac{\pi}{2}$ pulse is applied with a phase that is different between the two states. We measure the state of both qubits again and expect to get a $50-50$ population distribution of qubit #1 and a Ramsey fringe for qubit #2. After operating with a global $\frac{\pi}{2}$ pulse, the second qubit state is

$$e^{i\frac{\pi}{4}(\cos(\varphi)\sigma_x + i\sin(\varphi)\sigma_y)}\left(|S\rangle + |D\rangle\right)$$

Projecting this state on the dark state and calculating the population:

$$
\begin{aligned}
|\langle D|\psi\rangle|^2 &= \left|\langle D|\, e^{i\frac{\pi}{4}(\cos(\varphi)\sigma_x + i\sin(\varphi)\sigma_y)}\,(|S\rangle + |D\rangle)\right|^2 \\
&= \left|\langle D|\cos\left(\frac{\pi}{4}\right) + i\sin\left(\frac{\pi}{4}\right)(\cos(\varphi)\,\sigma_x + i\sin(\varphi)\,\sigma_y)\,(|S\rangle + |D\rangle)\right|^2 \\
&= \frac{1}{2}\,(1 - \sin(\varphi))
\end{aligned}
$$

doing the same with $\varphi + \pi$ phase:

$$
\begin{aligned}
|\langle D|\psi\rangle|^2 &= \left|\langle D|\, e^{i\frac{\pi}{4}(\cos(\varphi+\pi)\sigma_x + i\sin(\varphi+\pi)\sigma_y)}\,(|S\rangle - |D\rangle)\right|^2 \\
&= \left|\langle D|\cos\left(\frac{\pi}{4}\right) + i\sin\left(\frac{\pi}{4}\right)(\cos(\varphi+\pi)\,\sigma_x + i\sin(\varphi+\pi)\,\sigma_y)\,(|S\rangle - |D\rangle)\right|^2 \\
&= \frac{1}{2}\,(1 - \sin(\phi))
\end{aligned}
$$

We can see from this calculation that for the second qubit, we expect to get a fringe that will behave as a regular Ramsey fringe: a sine function with a 2π periodicity. Figure 25 represents the experimental sequence and figure 26 the results.

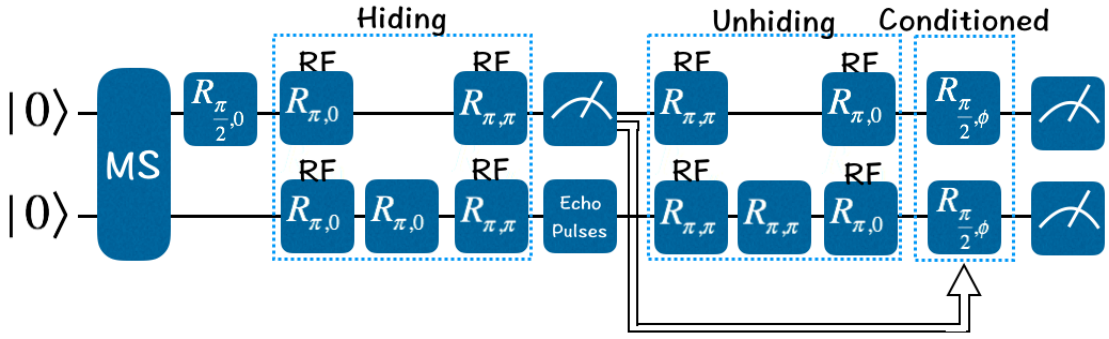

Figure 25: **Circuit drawing of the experimental sequence**.

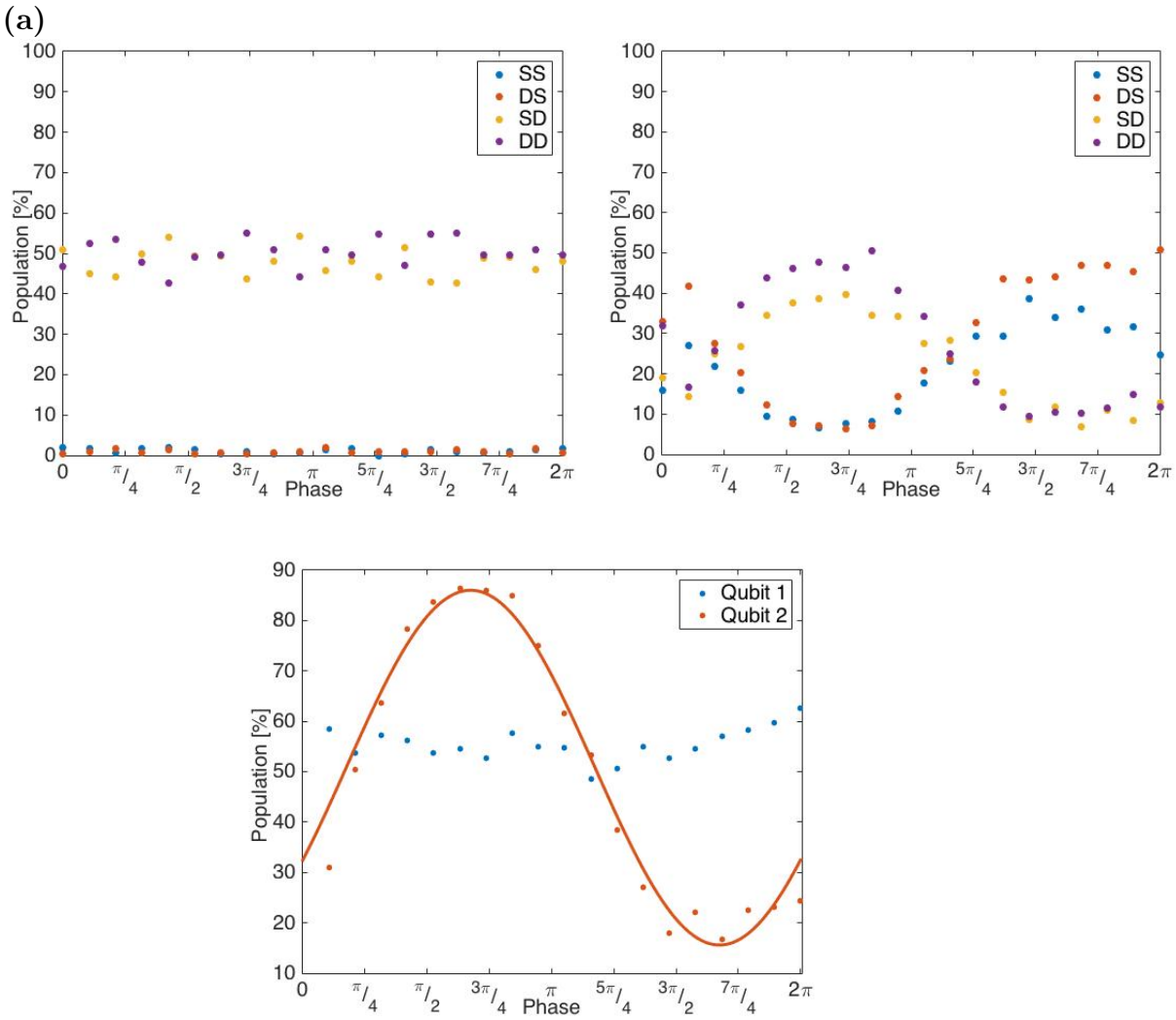

Figure 26: **Coherent feedback** performed on entangled qubits. **Left:** measurement after hiding qubit #2. **Right:** qubit #1 is the measured qubit and after the measurement collapses to one of both states - $|S\rangle$ or $|D\rangle$. After detecting this state, a conditioned $\frac{\pi}{2}$ pulse was applied with a phase φ or $\varphi + \pi$ according to the state. Qubit #2 is the hidden qubit and is measured only during the second measurement. After the second measurement, if the second ion is measured in the bright state - $|S\rangle$ (or a dark state $|D\rangle$), the first ion is projected onto $\frac{1}{\sqrt{2}}(|S\rangle + |D\rangle)$. This is due to the conditioned $\frac{\pi}{2}$ global pulse, thus qubit #1 will be found in an equal superposition. Qubit #2, on the other hand, shows a Ramsey fringe with a contrast of 70 (meaning the process's fidelity 85%). The fidelity is affected mainly during the time that the second qubit spends in the $|D\rangle$ manifold, where it can decohere due to magnetic noise. **Bottom:** Sum of the results for each qubit, where the y-axis represents the qubits' dark state population in percentages. We can see the Ramsey fringe of the second qubit, whereas the first qubit population is close to 50%. When no feedback is applied, we get an expected constant behavior around 50% for both qubits. Each data point represents the average of 300 repetitions, with 50 Hz trigger and 4 echo pulses on the hidden ion during the measurement.

6 Summary

This work presents the integration of a new classical control system into our lab that allows us to access the ions measurement outcome in real-time, analyzes the image data on the fly, determines the state of the ions followed by an adaptive feedback scheme that is pre-programmed. This scheme allowed us to coherently control the ions and perform conditional experiments with a fidelity of around $\sim 82\%$. Prior to the building and integration of the live readout system, the processing of the images was limited to the end of the experiment. The ability to coherently and conditionally control trapped ions is advancing our lab one step closer to performing quantum error correction protocols and to a fault-tolerant quantum computer. Although some improvements are required, the demonstration of quantum feedback is an important milestone. Quantum error correction protocols usually require the ability to act on a qubit according to the syndrome measurement outcome of the auxiliary qubit within a time scale much shorter than the coherence time of the qubits. We have demonstrated this kind of operation with two entangled ions, where we have measured one ion that collapsed the second ion to a superposition without losing its coherence - shown as a Ramsey fringe. Quantum error correction is not the only QIP experiment that can enjoy the benefits of having the ability to perform live feedback. Some ideas to preform experiments suggested in 6.2.

6.1 Improvements

The system is not perfect, and in order to perform complicated and long algorithms, the quantum feedback needs to be robust and fast. During this work, we have encountered a few major bottlenecks that affected our ability to perform very high fidelity live readout and feedback. The most significant ones are the exposure and readout time - they are very long compared to our coherence time. Two significant physical properties limit the exposure time: the first is the numerical aperture, which eventually sets the number of photons collected for each unit of time. The second is the camera limitations such as dark current and shot noise. The solution for both of these problems is possible but complicated and will require a major upgrade in the lab imaging set up (get a bigger objective lens or\and change the camera). Another bottleneck is the readout time. Using our EMCCD camera - Andor iXon ultra 879, our readout time is limited due to the size of the CCD and the fact that the technology is a frame transfer technology. This fact puts a lower bound on the readout time at hundreds of microseconds for a minimal

number of rows required for the ion detection. The readout time will always be a limiting factor and can be reduced using binning, smaller ROI, or a different EMCCD camera with a faster vertical shift rate and maybe a smaller CCD. One major improvement will be increasing our coherence time by, e.g., mu-metal shield placed around the ion trap. Another upgrade to be done regarding the connections of the hardware, there is a need for a robust "black box" hardware that will contain all of the FPGA cards, cables connecting them, and RF source control.

6.2 Outlook

Live feedback can be used for more than just quantum error correction codes that sometimes require a large number of ions, or complicated and long codes that are hard to execute due to decoherence and noise, but also for some more exotic experiments, that some of them are listed below.

Ramsey teleportation Quantum teleportation is the complete transfer of information from one particle to another (or from Alice to Bob). Generally, this process requires an infinite amount of information even to transfer a "simple" system such as one qubit. In quantum mechanics, a measurement immediately alters the state of the system while yielding at most one bit of information. At face value, teleportation seems to be impossible given these facts, but using quantum entanglement combined with classical communication, the idea of teleporting information came to life [54]. Three ions are needed to perform teleportation. Two of them prepared in a maximally entangled state: Alice and Bob each have one of the pair particles. Alice possesses the third qubit (can be treated as the auxiliary qubit), and both of Alice's qubits are entangled. Measuring the auxiliary qubit in a Bell state basis will leave Bob with one of four possible outcomes. Transferring Alice's measurement information (classically) to Bob, will allow him to reconstruct his state entirely, and by that, the teleportation will be completed. With trapped ions, quantum teleportation has been shown in several experiments, such as [55, 56]. In both of these experiments, published back-to-cack, deterministic teleportation was demonstrated for the first time. Quantum gate teleportation was also shown in [57]. Another quantity that can be teleported is the qubits accumulated phase due to the presence of a magnetic field. The teleportation experiment will be as a regular teleportation sequence just that the transported information will be about the phase. The operation to complete the teleportation will be the correcting of the phase, and a measurement in Bob's side after performing the correct gate with a phase scan that will result

in a Ramsey fringe. A problem can arise due to a magnetic field gradient that can affect differently on the Alice's and Bob's qubits (ions in a Paul trap) because they have a different location and will feel different magnetic fields, thus accumulate different phase.

Quantum neuron This experiment follows the article in [58]. The building blocks of an artificial neural network is a neuron that receives multiple (n) input signals x_i, integrally combines them, and applies a nonlinear function to the resulting weighted sum, which is the output value $a = \sigma \sum_{i=1}^{n} \omega_i x_i$. Here σ is the nonlinear activation function. There is a difficulty in generalizing this to the quantum regime because of the linear nature of quantum mechanics colliding with the need to implement a nonlinear activation function, which is a significant part of a neural network. The article mentioned offers a *quantum neuron* as a building block to a quantum neural network - a device or algorithm that will combine both of the unique features of the quantum nature and neural networks.

The main idea behind a quantum neuron is a quantum circuit that operates on three qubits with a repeat until success (RUS) mechanism. This mechanism depends on the measurement outcome of the auxiliary qubit (which is possible with the live feedback implemented in this work). The RUS will be until we measure $|0\rangle$. Our measurement result will be corrected by understanding the angle of rotation that was done and apply the opposite. (for example, if we will measure $|1\rangle$, a $R_y(-\pi/2)$ rotation is needed). The goal is to realize a form of threshold behavior on the rotation angle θ: if $\theta > \frac{\pi}{4}$, we would like the output qubit to be as close to $|1\rangle$ as possible ($R_y(\pi)|0\rangle = |1\rangle$). If $\theta < \frac{\pi}{4}$,we want our state to be$|0\rangle$ ($R_y(0)|0\rangle = |0\rangle$). On each RUS iteration, we are moving the input angle θ to the attractor that can be 0 or $\frac{\pi}{2}$. This depends if θ is greater than the threshold or not. The rotation angle θ can be mapped to an activation function q, for example, a step function or sigmoid such as $q(\varphi) = \arctan(\tan^2 \varphi)$. An example of this circuit can be shown in figure 27.

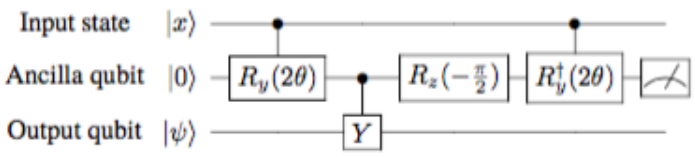

Figure 27: **Repeat until success** circuit for a rotation angle φ. [taken from figure 1 in [58]. Here we use three different qubits. The input qubit state can be initialized to any required state.

Shor's three qubit repetition code This experiment was done in trapped ions in [15]. The three-qubit Shor's repetition code is a quantum error correction code that can correct one error. It can be done using an induced error and a correction scheme where the measurement is at the end of each repetition. Using measurement, and the live feedback system the following scheme can conduct this experiment: encode a logic qubit into a subspace that is spanned by $\{|000\rangle, |111\rangle\}$ (encoding the information as $\alpha|000\rangle + \beta|111\rangle$). An error process will map the sub-space where the encoded information is, to an orthogonal subspace (that keeps the orthogonality of the previous subspace such as $\{|100\rangle, |011\rangle\}$) for each error thus not distorting the quantum information. Knowing which subspace the system is, will enable the correction of the error by applying the revers error operation. This process can be also done to a linear combination of the subspace above (e.g. $\frac{1}{\sqrt{2}}(|000\rangle + |111\rangle)$ and $\frac{1}{\sqrt{2}}(|000\rangle - |111\rangle)$) making it possible to correct phase flip errors.

References

[1] Peter W. Shor. Polynomial-time algorithms for prime factorization and discrete logarithms on a quantum computer. *SIAM Journal on Computing*, 26(5):1484–1509, 1997. arXiv:9508027, doi:10.1137/S0097539795293172.

[2] David P. DiVincenzo. The physical implementation of quantum computation. *Fortschritte der Physik*, 48(9-11):771–783, 2000. arXiv:0002077, doi:10.1002/1521-3978(200009)48:9/11<771::AID-PROP771>3.0.CO;2-E.

[3] D J Wineland, C Monroe, W M Itano, D Leibfried, B E King, and D M Meekhof. Experimental Issues in Coherent Quantum-State Manipulation of Trapped Atomic Ions. *Journal of Research of the National Institute of Standards and Technology*, 103(3):259–328, 1998. URL: http://www.nist.gov/jres, arXiv:9710025, doi:10.6028/jres.103.019.

[4] J. I. Cirac and P. Zoller. Quantum computations with cold trapped ions. *Physical Review Letters*, 74(20):4091–4094, 1995. doi:10.1103/PhysRevLett.74.4091.

[5] D. J. Wineland and Wayne M. Itano. Laser cooling of atoms. *Physical Review A*, 20(4):1521–1540, 1979. doi:10.1103/PhysRevA.20.1521.

[6] Dorit Aharonov and Michael Ben-Or. Fault-tolerant quantum computation with constant overhead. *Quantum Information and Computation*, 14(15-16):1338–1372, 2014. arXiv:1310.2984.

[7] Frank Arute, Kunal Arya, Ryan Babbush, Dave Bacon, Joseph C. Bardin, Rami Barends, Rupak Biswas, Sergio Boixo, Fernando G.S.L. Brandao, David A. Buell, Brian Burkett, Yu Chen, Zijun Chen, Ben Chiaro, Roberto Collins, William Courtney, Andrew Dunsworth, Edward Farhi, Brooks Foxen, Austin Fowler, Craig Gidney, Marissa Giustina, Rob Graff, Keith Guerin, Steve Habegger, Matthew P. Harrigan, Michael J. Hartmann, Alan Ho, Markus Hoffmann, Trent Huang, Travis S. Humble, Sergei V. Isakov, Evan Jeffrey, Zhang Jiang, Dvir Kafri, Kostyantyn Kechedzhi, Julian Kelly, Paul V. Klimov, Sergey Knysh, Alexander Korotkov, Fedor Kostritsa, David Landhuis, Mike Lindmark, Erik Lucero, Dmitry Lyakh, Salvatore Mandrà, Jarrod R. McClean, Matthew McEwen, Anthony Megrant, Xiao Mi, Kristel Michielsen, Masoud Mohseni, Josh Mutus, Ofer Naaman, Matthew Neeley, Charles Neill, Murphy Yuezhen Niu, Eric Ostby, Andre Petukhov, John C. Platt, Chris Quintana, Eleanor G. Rieffel, Pedram Roushan, Nicholas C.

Rubin, Daniel Sank, Kevin J. Satzinger, Vadim Smelyanskiy, Kevin J. Sung, Matthew D. Trevithick, Amit Vainsencher, Benjamin Villalonga, Theodore White, Z. Jamie Yao, Ping Yeh, Adam Zalcman, Hartmut Neven, and John M. Martinis. Quantum supremacy using a programmable superconducting processor. *Nature*, 574(7779):505–510, oct 2019. arXiv:1911.00577, doi:10.1038/s41586-019-1666-5.

[8] Daniel Gottesman. Fault-Tolerant Quantum Computation. 2007.

[9] D. Nigg, M. Müller, E. A. Martinez, P. Schindler, M. Hennrich, T. Monz, M. A. Martin-Delgado, and R. Blatt. Quantum computations on a topologically encoded qubit. *Science*, 345(6194):302–305, 2014. arXiv:1403.5426v1, doi:10.1126/science.1253742.

[10] Philipp Schindler, Julio T. Barreiro, Thomas Monz, Volckmar Nebendahl, Daniel Nigg, Michael Chwalla, Markus Hennrich, and Rainer Blatt. Experimental repetitive quantum error correction. *Science*, 332(6033):1059–1061, may 2011. doi:10.1126/science.1203329.

[11] Philipp Schindler, Daniel Nigg, Thomas Monz, Julio T. Barreiro, Esteban Martinez, Shannon X. Wang, Stephan Quint, Matthias F. Brandl, Volckmar Nebendahl, Christian F. Roos, Michael Chwalla, Markus Hennrich, and Rainer Blatt. A quantum information processor with trapped ions. *New Journal of Physics*, 15, 2013. arXiv:1308.3096, doi:10.1088/1367-2630/15/12/123012.

[12] H. Bernien, B. Hensen, W. Pfaff, G. Koolstra, M. S. Blok, L. Robledo, T. H. Taminiau, M. Markham, D. J. Twitchen, L. Childress, and R. Hanson. Heralded entanglement between solid-state qubits separated by three metres. *Nature*, 497(7447):86–90, apr 2013. arXiv:1212.6136, doi:10.1038/nature12016.

[13] D. G Cory, Price M.D., W. Maas, E. Knill, R. Laflamm, W. H. Zurek, T. F. Havel, and S. S. Somaroo. Experimental quantum error correction. *Quantum Error Correction*, 9780521897:508–518, 2012. URL: https://www.cambridge.org/core/product/identifier/CBO9781139034807A173/type/book{_}part, doi:10.1017/CBO9781139034807.023.

[14] E. Knill, R. Laflamm, A. Ashikhmin, H. Barnum, L. Viola, and W. H. Zurek. Introduction to quantum error correction. *Quantum Error Correction*, 9780521897:46–77, 2012. doi:10.1017/CBO9781139034807.004.

[15] J Chiaverini, D Leibfried, T Schaetz, M D Barrett, R B Blakestad, J Britton, W M Itano, J D Jost, E Knill, C Langer, R Ozeri, and D J Wineland. Realization of quantum error correction. *Nature*, 432(7017):602–605, 2004. URL: www.nature.com/nature, doi:10.1038/nature03074.

[16] Norbert M. Linke, Mauricio Gutierrez, Kevin A. Landsman, Caroline Figgatt, Shantanu Debnath, Kenneth R. Brown, and Christopher Monroe. Fault-tolerant quantum error detection. *Science Advances*, 3(10), 2017. URL: http://advances.sciencemag.org/, arXiv:1611.06946, doi:10.1126/sciadv.1701074.

[17] Daniel Gottesman. Quantum fault tolerance in small experiments. oct 2016. URL: http://arxiv.org/abs/1610.03507, arXiv:1610.03507.

[18] Daniel Gottesman. An introduction to quantum error correction and fault-tolerant quantum computation. pages 13–58, apr 2010. URL: http://arxiv.org/abs/0904.2557, arXiv:0904.2557, doi:10.1090/psapm/068/2762145.

[19] N. Akerman, S. Kotler, Y. Glickman, and R. Ozeri. Reversal of photon-scattering errors in atomic qubits. *Physical Review Letters*, 109(10), sep 2012. arXiv:1111.1622, doi:10.1103/PhysRevLett.109.103601.

[20] M. Riebe, T. Monz, K. Kim, A. S. Villar, P. Schindler, M. Chwalla, M. Hennrich, and R. Blatt. Deterministic entanglement swapping with an ion-trap quantum computer. *Nature Physics*, 4(11):839–842, 2008. doi:10.1038/nphys1107.

[21] V. Negnevitsky, M. Marinelli, K. K. Mehta, H. Y. Lo, C. Flühmann, and J. P. Home. Repeated multi-qubit readout and feedback with a mixed-species trapped-ion register. *Nature*, 563(7732):527–531, nov 2018. arXiv:1804.09703, doi:10.1038/s41586-018-0668-z.

[22] D B Hume, T Rosenband, and D J Wineland. High-fidelity adaptive qubit detection through repetitive quantum nondemolition measurements. *Physical Review Letters*, 99(12), 2007. doi:10.1103/PhysRevLett.99.120502.

[23] J. Cramer, N. Kalb, M. A. Rol, B. Hensen, M. S. Blok, M. Markham, D. J. Twitchen, R. Hanson, and T. H. Taminiau. Repeated quantum error correction on a continuously encoded qubit by real-time feedback. *Nature Communications*, 7, may 2016. URL: http://arxiv.org/abs/1912.09410, arXiv:1508.01388, doi:10.1038/ncomms11526.

[24] Adriano Barenco, Charles H Bennett, Richard Cleve, David P Divincenzo, Norman Margolus, Peter Shor, Tycho Sleator, John A. Smolin, and Harald Weinfurter. Elementary gates for quantum computation. *Physical Review A*, 52(5):3457–3467, 1995. arXiv:9503016, doi:10.1103/PhysRevA.52.3457.

[25] Tom Manovitz. *Individual Addressing and imaging of ions in a paul trap*. PhD thesis, 2016.

[26] Roee Ozeri. The trapped-ion qubit tool box. *Contemporary Physics*, 52(6):531–550, nov 2011. doi:10.1080/00107514.2011.603578.

[27] Anders Sørensen and Klaus Mølmer. Entanglement and quantum computation with ions in thermal motion. *Physical Review A - Atomic, Molecular, and Optical Physics*, 62(2):11, 2000. arXiv:0002024, doi:10.1103/PhysRevA.62.022311.

[28] Yotam Shapira. *Robust entanglement of trapped ion qubits*. PhD thesis, 2017.

[29] Yotam Shapira, Ravid Shaniv, Tom Manovitz, Nitzan Akerman, and Roee Ozeri. Robust Entanglement Gates for Trapped-Ion Qubits. *Physical Review Letters*, 121(18), may 2018. URL: http://arxiv.org/abs/1805.06806http://dx.doi.org/10.1103/PhysRevLett.121.180502, arXiv:1805.06806, doi:10.1103/PhysRevLett.121.180502.

[30] Nitzan Akerman. *Trapped ions and free photons*. PhD thesis, 2012.

[31] Ravid Shaniv. *Spectral noise analysis of a narrow linewidth laser*. PhD thesis, 2015.

[32] Anna Keselman. *High Fidelity Ion Qubit State Detection*. PhD thesis, 2010.

[33] Regina Lechner, Christine Maier, Cornelius Hempel, Petar Jurcevic, Ben P. Lanyon, Thomas Monz, Michael Brownnutt, Rainer Blatt, and Christian F. Roos. Electromagnetically-induced-transparency ground-state cooling of long ion strings. *Physical Review A*, 93(5), 2016. URL: http://arxiv.org/abs/1603.05568{%}0Ahttp://dx.doi.org/10.1103/PhysRevA.93.053401, arXiv:1603.05568, doi:10.1103/PhysRevA.93.053401.

[34] J. Eschner, C. Keitel, and G. Morigi. Laser cooling using electromagnetically induced transparency. *Conference on Quantum Electronics and Laser Science (QELS) - Technical Digest Series*, pages 63–64, 2000.

[35] C S. Roos, D Leibfried, A Mundt, F Schmidt-Kaler, J Eschner, and R Blatt. Experimental Demonstration of Ground State Laser Cooling with Electromagnetically Induced Transparency. *Physical Review Letters*, 85(26):5547–5550, 2000. doi:10.1103/PhysRevLett.85.5547.

[36] D. J. Wineland and H. G. Dehmelt. Principles of the stored ion calorimeter. *Journal of Applied Physics*, 46(2):919–930, 1975. URL: https://doi.org/10.1063/1.321602, doi:10.1063/1.321602.

[37] Andor Technology. iXon Ultra Hardware Guide. Technical report, 2013.

[38] E2v. CCD97-00 Back Illuminated 2-Phase IMO Series Electron Multiplying CCD Sensor. Technical report. URL: www.e2vtechnologies.com.

[39] Robert N. Tubbs. Lucky Exposures: Diffraction limited astronomical imaging through the atmosphere. (September), 2003. URL: http://arxiv.org/abs/astro-ph/0311481, arXiv:0311481.

[40] A. G. Basden, C. A. Haniff, and C. D. Mackay. Photon counting strategies with low-light-level CCDs. *Monthly Notices of the Royal Astronomical Society*, 345(3):985–991, 2003. arXiv:0307305, doi:10.1046/j.1365-8711.2003.07020.x.

[41] Alice Heather Burrell. *High Fidelity Readout of Trapped Ion Qubits*. PhD thesis, 2010.

[42] Michael Hirsch, Richard J. Wareham, Marisa L. Martin-Fernandez, Michael P. Hobson, and Daniel J. Rolfe. A Stochastic Model for Electron Multiplication Charge-Coupled Devices - From Theory to Practice. *PLoS ONE*, 8(1), jan 2013. doi:10.1371/journal.pone.0053671.

[43] D. F.V. James. Quantum dynamics of cold trapped ions with application to quantum computation. *Applied Physics B: Lasers and Optics*, 66(2):181–190, 1998. arXiv:9702053, doi:10.1007/s003400050373.

[44] Edmund Optics Inc. Imaging Electronics 101: Understanding Camera Sensors for Machine Vision Applications, 2014. URL: http://www.edmundoptics.com/technical-resources-center/imaging/understanding-camera-sensors-for-machine-vision-applications/.

[45] Basler Vision Technologies. Camera Link Technology Brief. Technical report, 2001. URL: www.basler-mvc.com.

[46] National Semiconductor's LVDS group. LVDS Owner's Manual Low-Voltage Differential Signaling National Semiconductor. Technical report, 2004.

[47] Frame Grabbers. Camera Link Specifications of the Camera Link Interface Standard for Digital Cameras. (January):1–48, 2004.

[48] Nick Schwegler. *Towards Low-Latency Parallel Readout of Multiple Trapped Ions*. PhD thesis, 2018.

[49] Vision-Basler. Camera Link Technology Brief Subject to Change Without Notice. Technical report, 2001. URL: `www.basler-mvc.com`.

[50] National instruments. NI PCIe-1473R User Guide and Specifications. Technical report.

[51] N. Akerman, Y. Glickman, S. Kotler, A. Keselman, and R. Ozeri. Quantum control of 88Sr+ in a miniature linear Paul trap. *Applied Physics B: Lasers and Optics*, 107(4):1167–1174, 2012. `doi:10.1007/s00340-011-4807-6`.

[52] Mark Stanford Robbins and Benjamin James Hadwen. The noise performance of electron multiplying charge-coupled devices. *IEEE Transactions on Electron Devices*, 50(5):1227–1232, may 2003. `doi:10.1109/TED.2003.813462`.

[53] Nitzan Akerman, Nir Navon, Shlomi Kotler, Yinnon Glickman, and Roee Ozeri. Universal gate-set for trapped-ion qubits using a narrow linewidth diode laser. *New Journal of Physics*, 17(11), 2015. `doi:10.1088/1367-2630/17/11/113060`.

[54] Charles H Bennett, Gilles Brassard, Claude Crépeau, Richard Jozsa, Asher Peres, and William K Wootters. Teleporting an unknown quantum state via dual classical and Einstein-Podolsky-Rosen channels. *Physical Review Letters*, 70(13):1895–1899, 1993. `doi:10.1103/PhysRevLett.70.1895`.

[55] M. Riebe, H. Häffner, C. F. Roos, W. Hänsel, J. Benheim, G. P.T. Lancaster, T. W. Körber, C. Becher, F. Schmidt-Kaler, D. F.V. James, and R. Blatt. Deterministic quantum teleportation with atoms. *Nature*, 429(6993):734–737, jun 2004. `doi:10.1038/nature02570`.

[56] M. D. Barrett, J. Chiaverini, T. Schaetz, J. Britton, W. M. Itano, J. D. Jost, E. Knill, C. Langer, D. Leibfried, R. Ozeri, and D. J. Wineland. Deterministic quantum teleportation of atomic qubits. *Nature*, 429(6993):737–739, jun 2004. `doi:10.1038/nature02608`.

[57] Yong Wan, Daniel Kienzler, Stephen D. Erickson, Karl H. Mayer, Ting Rei Tan, Jenny J. Wu, Hilma M. Vasconcelos, Scott Glancy, Emanuel Knill, David J. Wineland, Andrew C. Wilson, and Dietrich Leibfried. Quantum gate teleportation between separated qubits in a trapped-ion processor. *Science*, 364(6443):875–878, may 2019. arXiv:1902.02891, doi:10.1126/science.aaw9415.

[58] Francesco Tacchino, Chiara Macchiavello, Dario Gerace, and Daniele Bajoni. An artificial neuron implemented on an actual quantum processor. *npj Quantum Information*, 5(1), 2019. URL: https://doi.org/10.1038/s41534-019-0140-4, arXiv:1811.02266, doi:10.1038/s41534-019-0140-4.